On chip optical sensing

PhD candidate: Sara Perotto

Supervisor: dr. Francesco De Angelis

Table of Contents

Introduction

Single particle detection is currently a hot topic in several scientific communities from medicine to pharmacology, from nanophysics to chemistry. The interest in this subject is not purely limited to scientific research, in fact the development of increasingly sensitive biosensing techniques capable of detection sensitivity down to the individual molecule has significant repercussions in the world of medicine and diagnostics. One of the major issues of recent years is, for example, early detection of different diseases, from inflammatory state to cancer. Within this theme, liquid biopsy, that is the ability to detect certain biomarkers in biological fluids (saliva, urine or blood), is emerging as a power tool for monitoring and prognosis and as a valid alternative to more invasive tissue biopsies.

The microscopic and spectroscopic techniques currently in use to measure single particles or molecules have some limitations that prevent their spread on a large scale. For example, they are time-consuming and often involve steps of purification and labeling, furthermore they generally require expensive instrumentation and highly qualified personnel. The global trend is to move towards fast, specific and low-cost systems for detecting individual particles in complex and heterogeneous media, with a growing demand for technologies based on robust and affordable nanostructures, able to compete with larger instruments. This has paved the way for a boom in biosensor research.

Depending on the transduction principle, biosensors can be classified into different categories such as mechanical, acoustic, electrochemical, optical, etc. Among these many possibilities, optical biosensors offer the advantages of very high sensitivity, potentially direct operation (no pre-processing of the sample required) and can provide multiplexed detection within a single device. In addition, they are free from electromagnetic interference, can perform real time and remote sensing. For these reasons, in recent years optical sensors for single particle detection and analysis have been proposed for biomedical research, air, water and food control, as well as security and defense. In general, there are two detection protocols that can be implemented in optical biosensing: label-free and fluorescence-based detection. Both protocols are widely used in optical sensors and provide essential and complementary information regarding interactions between biomolecules, which makes optical sensors more versatile than other types of sensing technologies.

Nowadays, the most common optical biosensors are based on Surface Plasmon Resonance (SPR) techniques. This technique is based on the plasmon resonant oscillation at the metal-dielectric interface. The local dielectric constant varies when a binding event takes place and this variation results in a change in the plasmon mode. Since the plasmon modes decay exponentially in the metal and dielectric media, only the events in the first layers will be detected (200/300 nm depending on the working wavelength). The SPR technique is then used to monitor the interaction between antibodies and antigens within the first monolayers covering the sensor surface and gives binding and kinetic information. However, the subject is in full expansion and several approaches are under consideration, among which one of the most promising is the use of integrated optical devices (IO).

Integrated Optics (IO) is a technology born as part of photonics with the aim of developing light wave circuits for complex optical operations. One of the most important points is that it uses a very well developed and validated technology, namely the silicon microelectronics industry. This offers standardized and well-known manufacturing processes, with the consequent possibility of lowering production costs, adding mechanical stability and achieving high levels of integration.

In fact, they are able to operate in real samples (such as blood or urine) offering relevant sensitivities even in unlabeled systems. In addition, IO sensor arrays for multiplexed analysis can be integrated with microfluidic systems and more generally in laboratory on chip (LOC) platforms, providing a cost-effective production and miniaturization. In this sense, IO-based biosensor devices have great potential for building devices that can operate in parallel, making real-time multiplex recognition possible.

By aiming for a low-cost, high-performance optical production system, the materials play a key role in IO. Silicon is the most widely used material, incorporating a whole family of related materials such as silicon nitride, polysilicon and silicon dioxide. In fact, IO usually refers to the multi-layer silicon-on-insulator structure, namely SOI, consisting in silicon layer deposited onto an insulator layer generally made of SiO_2. Within this platform, the model is suitably transferred to the top layer of silicon by lithographic and dry etching techniques. However, recently, different materials and manufacturing processes are being studied, for example spinnable materials with high refractive index and the use of nanoimprint lithography.

Several configurations are currently being studied, which differ in the type of analysis (interferometry, absorption, etc.), geometry (such as waveguides, microspheres and nanoparticles) and material (e.g. dielectrics or metals in the case of plasmonic approach).

In particular, the WGM resonators (Whispering Gallery Modes (WGM)), in addition to their exceptional sensitivity, show several technological strengths such as robustness and resistance in an aqueous environment, scalability, multiplexing and ease of integration in microfluidic devices for parallel analysis. Depending on the specific application, both label-free detection schemes and specifically functionalized detection schemes can be implemented. In addition, when combined with optical capture and microfluidic systems, these nanosensors allow the integration of different spectroscopic techniques such as Raman and fluorescence-based spectroscopy. In this way, it would be possible to perform a complete physical-chemical characterization of each individual particle.

Evidence of the applicability of dielectric resonant structures in the segment of sensing devices currently in use is the presence on the market of the first examples, such as Genalyte, a U.S. company that uses photonic ring resonators to perform immunoassays through the detection of refractive index changes. Their device, currently in the final stage of the development and validation process, boasts a consistent menu of 62 tests and an assay that can give medical results in just 15 minutes.

Despite the high Q-factor and unique sensitivity, when dealing with single particle detection, WGM resonators have some limitations. For example, the limited resonance shift due to the low modal volume and intensity of the sensing field, which consists of the evanescent tail of the field coming out of the surface of the resonator.

In addition, conventional biochemical sensing techniques using optical microresonators typically require a precision spectrum scanning system, such as a wavelength tunable diode laser. In fact, two methods can be used to quantitatively obtain real-time analyte information on the surface of the microresonator. One is to monitor the ultra-high quality (ultra-high Q) resonance wavelength shifts in the transmission spectrum by scanning the wavelength of the incoming laser near the resonance. The other is to monitor the change in transmission intensity around a resonance in cavities at a fixed wavelength.

In this work we present an innovative design for a biosensor able to overcome some of the current limits in nanoparticle and molecules detection with WGMs. Deferring the detailed description and

analysis of the model to the next pages, it consists in a resonant structure in silicon nitride with a hole that crosses the entire depth of the waveguide. This allows the co-location in a nanometric volume of the target particle and a highly confined electromagnetic field. This design is very versatile, permitting to work in label-free and labeled configuration. In the label-free configuration, the purely photonic characteristics of the structure are leveraged, resulting in enhanced sensitivity. In the labeled configuration, the nm-sized hole acts as a point-like source allowing single particle detection by mean of fluorescence spectroscopy.

Chapter 1 gives a brief overview of the different technologies and materials developed in the field of Integrated Optics, with particular attention to the application of biosensing and the state of the art of detecting single particles of different technologies.

Chapter 2 deals with the theoretical modelling of the sensing structure. We present a brief introduction of the principles underlying whispering gallery mode resonators and their main properties. Secondly, simulations and the theoretical explanation of the modeled structure are discussed.

In Chapter 3 we focus on the point-like source on-chip. Besides the optical characterization of the device, experimental results are discussed together with the comparison between straight waveguides and resonating structures.

Chapter 4 presents the results obtained by fluorescence-based techniques demonstrating the possibility to perform single particle detection in high dense media. A quick discussion on the fluorescence correlation spectroscopy (FCS) measurements is also reported.

Finally, a brief conclusion of the overall work is given with interesting perspectives for future developments and applications.

Chapter 1
Integrated optics

This chapter provides an overview of integrated optics devices, giving an insight into the different approaches currently being studied. As one of the most active areas of research in recent decades, it is a challenging task to provide a complete and exhaustive description of all the techniques currently being studied. Here we focus on the most diffused and promising techniques, presenting their principle of operation and the state of the art of their use in biosensing applications with particular emphasis on the detection of individual particles.

1.1 Interferometric devices

Interferometric devices are quite common as they exhibit extremely low detection limits and meet the conditions of miniaturized, low-cost, label-free configuration.

In general, it reads the interference of two waves that have travelled different optical paths. The external source is coupled to the on-chip waveguide, which at some point splits into two parts and reunites after experimenting different optical paths. In biosensor application, one of the branches is used as a reference arm while the other acts as the detection arm, being exposed to external media.

So while the propagating wave in the reference branch will remain unchanged, the other will be sensitive to the external environment, undergoing a phase change related to the variation of the general system (bulk sensitivity) or to the binding of molecules on the surface (surface sensitivity). Therefore the variation introduced in the pattern of interference determined by the overlapping of the propagating modes of each pathway will depend on a change in the mass refractive index. In alternative, if the surface of the detection arm is previously functionalized with a receptor layer, the interference can be ascribed to a specific biomolecular interaction. The sensitivity of the system is proportional to the interaction length of the field with the external medium. It can therefore be increased by lengthening the sensitive region (active branch).

Several different interferometric configurations have been developed such as Mach–Zehnder [1], [2], Young [3], Hartman [4], and dual polarization interferometry [5], [6] and bimodal waveguide interferometers [7], [8]. Examples of IO solutions based on some of them are shown in Figure 31.

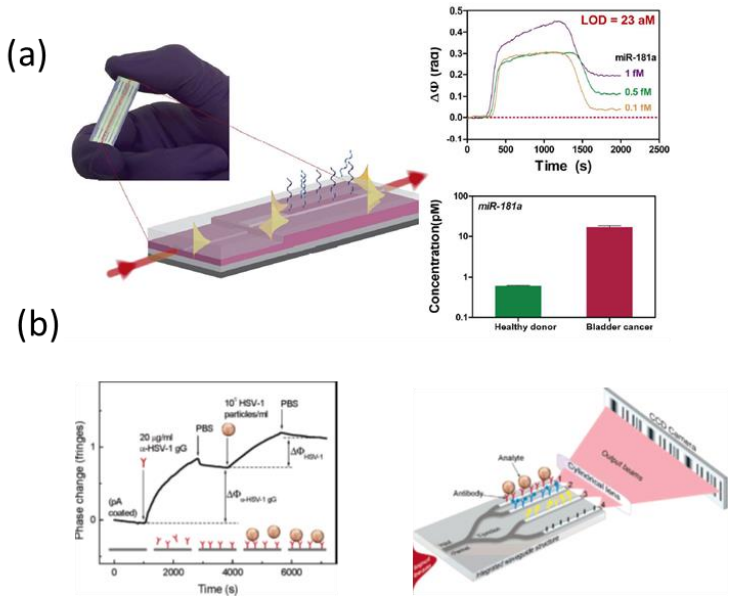

Figure 1 - IO solution for: (a) Bimodal Waveguide, taken from [8]. (b) Young interferometer, taken from [3]

Polymer-based interferometers have been proposed as an alternative to the classical dielectric solutions. Although responding to the requirements of cost-effective and large-scale production, the instability in buffer solution prevents their use in biological assays. Indeed the polymers proposed up to now present refractive index change due to water absorption.

1.2 Photonic crystals

Optical biosensors based on photonic crystals (PhC) have been deeply studied for their great ability to exhibit a strong confinement of light in a very small volume [9]–[11]. A photonic crystal has a properly designed periodic dielectric structure with a frequency that falls within the inspection light wavelength scale and which gives rise to interference phenomena. Such effects can strongly modulate the intensity and phase of probing electromagnetic waves and, if the dielectric contrast is sufficient and with an appropriate geometry, a photon band gap (PBG) can be generated [12].

The incident light whose wavelength is inside the photonic band gap cannot propagate through the photonic crystal and a wide bandgap emerges on the transmission (or reflection) spectrum. When a defect is introduced to locally disturb the periodic structure, a defect mode is formed. The light resonating with the defect mode can propagate into the photonic crystal resulting in a relatively strong peak within the bandgap on the transmission (or reflection) spectrum. The most important property of this structure is that, by appropriately arranging the periodicity and symmetry of the crystal of a specific material with its dielectric constant, it is possible to concentrate the light at a precise wavelength and in extremely small volumes, producing very high local electromagnetic field intensity in a microcavity that can be used for sensing applications.

As with most integrated optical devices, dielectric layers such as Si_3N_4, TiO_2, SiO_2 and the SOI structures emerge among the materials normally used [13]. Other materials generally used for the fabrication of planar PhC devices are heteroepitaxial layers, such as AlGaAs/GaAs and III-nitride compound layers. Furthermore, polymers, organic compounds and porous silicon have been also proposed for the fabrication of PhC sensors for organic vapour sensing [14].

PhC-based sensors can be efficiently integrated with microfluidic systems in order to achieve very high performance in ultra-compact chips [15]. Figure 2 shows the SEM pictograph and the transmission spectrum of a PhC

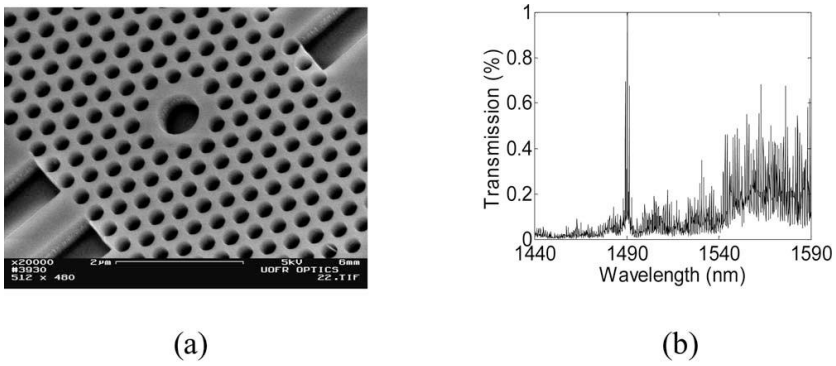

Figure 2 - (a) SEM image of a PhC and (b) relative transmission spectrum.

1.3 Dielectric resonators

Despite the high sensitivity and the extremely confined modal volume, the techniques presented so far are subject to certain limits, for example probability of detection is restricted by diffusion

limits. In fact, net of particular microfluidic structures, in single-pass optical devices the light interacts with the particle or the analyte in solution only once. To increase the probability that the analyte is detected, it is necessary to increase the physical length of the sensor. The trade-off between this solution and the need for a compact design for integration into the LoC platform has led to configurations such as spiral wavelengths, with interaction lengths of several millimeters concentrated in a small area of a few mm^2 [16].

The need for even more compact structures has led to the introduction of resonant microcavities. In sensors based on resonant structures, light confined to a cavity runs several times through it before being lost by scattering or radiation or being coupled out, thus significantly increasing the length of interaction. As will be further discussed, the propagation length depends on the material and the quality factor (Q) of the specific cavity. By increasing the quality factor of the resonant system it is possible to increase the effective interaction length.

High quality optical resonators have been deeply studied in recent years as one of the most promising technologies for ultra-sensitive and label-free biosensors [17]. In fact, they show extremely low losses and therefore an extremely long photon lifetime, together with high intracavity power. Whispering Gallery Mode (WGM) resonators show the highest Q-factor and several designs have been proposed [17], for example microspheres [18], ring resonators [19], [20], liquid-core optical ring resonator (LCORR) [21] and microtoroids [22], [23]. Not only the geometry, but also the material plays a fundamental role in these devices. It follows that depending on the geometry and the application, different dielectric materials have been exploited, ranging from silica to silicon and silicon nitride to polymers, to name a few.

It is possible to distinguish four main types of dielectric WGM resonators, examples of each of them are shown in Figure 3.

Microsphere resonators support resonances with extremely high quality factors up to 10^8–10^9 in the visible/near infrared region [17], [24]–[26] and are usually made of glass or polymers. Glass spherical cavities are generally fabricated by heating and stretching the extremity of an optical fiber, and are excited by the same supporting fiber or by another optical fiber brought in close proximity[27], [28]. Recently, new coupling schemes with microsphere resonators have also been used: they have been immobilized on a glass substrate and excited by total internal reflection [29], [30]. This approach helps to reduce the complexity of WGM systems, and is a very useful step for

the commercialization of optical biosensors. Thanks to their extremely sharp resonances, dielectric microspheres are among the best candidate for single molecule sensing.

Disks and microtoroids are fabricated in silicon, polymers or glass and exhibit high quality factors as high as 10^8 [31], [32]. In silicon and silicon dioxide, the fabrication process is articulated in several steps of photolithography, pattern transfer and dry etching, as described, for example, in [31]. Recent progress in the manufacture of all-glass toroids on-chips offers new possibilities for the large-scale production of high-quality toroidal resonators for biosensing. As with microsphere resonators, excitation is provided by an optical fiber that is brought close to the toroid.

Liquid-core optical ring resonator (LCORR) presents a quite different approach. A glass or plastic capillary with total diameters larger than 50 μm is coupled to the light source so that the travelling guided mode is confined in its wall and sense the fluid flowing inside by the internal evanescent tail [21], [33]–[37]. The typical quality factors are in the range 10^5–10^7.

Finally, disk resonators, ring and racetrack on silicon chip are widely studied, offering good quality factor and some practical advantages. Depending on the ring diameters and materials, the quality factors vary from 10^2 to 10^6 [17], [32], [38], [39]. A widely used platform is that of SOI wafers, i.e. silicon wafers where a silicon oxide buffer layer that separates the substrate from the silicon waveguide layer (hundreds of nm thick) placed on the top. Although that of SOI is historically the main diffused platform, micro-rings and disks can be fabricated with different materials including silicon, silicon nitride, glass or polymers.

Typical manufacturing techniques are UV lithography [40], electron-beam lithography [41] and focused-ion-beam lithography [42]. These include the ability to integrate multiple devices on a single chip, which is desirable for multiplex operation, and the stable coupling condition, thanks to the waveguide directly, which is directly etched on the platform. In addition, within the arrays, individual sensors can be used as internal reference, eliminating noise due to temperature fluctuations and non-specific molecular bonding events [20].

The first commercial biosensors based on ring resonators have already appeared on the market [43] and, together with the other families of photonic structures [44], [45], they have great potential for future applications in points of care and portable devices [46].

Given their great potentialities and their remarkable optical properties, purely dielectric WGM resonators have been investigated in detail over the last decade.[17], [47]–[49] A useful comparison of the most influential published works reported on WGM single particle detection, in terms of the main parameters and detection capabilities, can be found in are analyzed in [50].

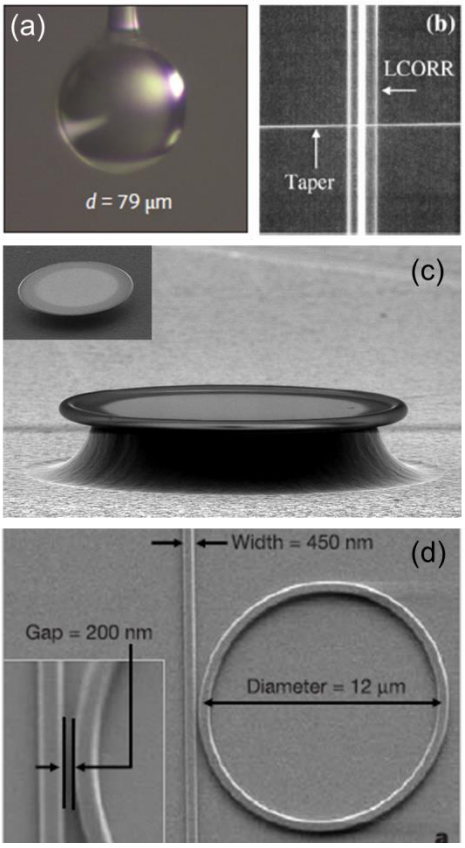

Figure 3- Several dielectric resonators are shown: (a) Optical picture of a glass microsphere resonator bound to an optical fiber [26]. (b) SEM pictograph of a capillary resonator [21]. (c) SEM pictograph of a fused silica toroidal cavity on a silica substrate [36]. (d) SEM pictograph of a silicon ring resonator on a silicon-on-insulator wafer [41].

An overview of the performance of the WGM photonic sensors is given in Figure 4. This is taken from Judith Su et al. [19], and can be referred to as the state of the art for the optical detection of single particles. The best reported result is the detection of human molecules of interleukin-2 (diameter of 4 nm) and nanobeads of SiO_2 (diameter of 5 nm) and with spectral shifts of the order of a few attometers, which correspond to approximately 1/1000 of the FWHM of resonance. This can be achieved by means of frequency-locking techniques. Rather than continuously sweeping the laser frequency to trace the resonance frequency of the WGM cavity, the laser frequency is set at the WGM resonance. This significantly reduces the noise associated to the measurement and also increases the sampling rate.

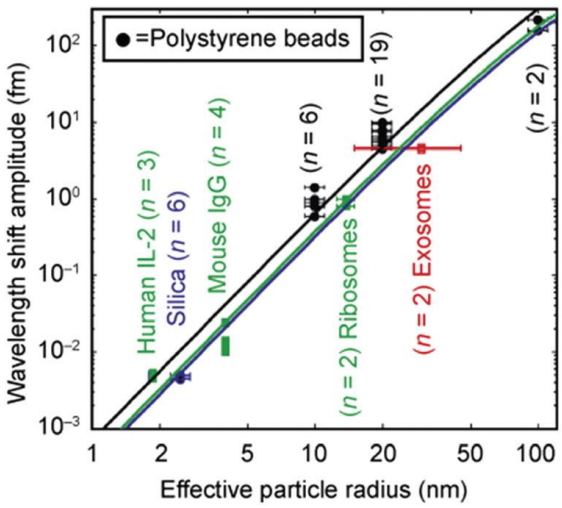

Figure 4 - State of the art for single particle detection using a purely photonic WGM resonator.By [23]

Another work of particular importance is that of Zhu and collaborators [51], Instead of looking at the displacement of the resonance, the authors count the particles and measure their size by monitoring the splitting of the resonance induced by the binding of the particles on the surface. This detection scheme demands WGM cavities with very high quality factors ($Q \sim 10^8$) and being a self-referenced method it reduces the spectral noise significantly.

It is worth noting that among the various WGM dielectric resonators, ring resonators have some inherent advantages that make them one of the best candidates for biosensing devices, such as compactness and ease of integration into planar chips. For this reason, many advances in the integration of these structures have been presented, such as multiplexed detection or improvements in microfluidics. Ring resonator arrays functionalized with clinically relevant biomarkers have also been used to develop LOC devices.

1.4 Hybrid photonic-plasmonic structures

In the last few years, in order to increase the sensitivity to the binding of very small objects, the integration of localized plasmonic structures in WGM resonators was proposed.

Metallic structures shows unique optical properties, for example when opportunely excited by light in visible or near infrared range, they can support surface plasmon resonances (SPR). That is, the incoming light excite the free electrons of metal inducing a collective in-phase oscillations. Although plasmonic nanostructures lack in high intrinsic quality factor, LSP resonances are

characterized by a high field confinement and strong enhancement. Furthermore the size of these hot-spots of electromagnetic energy density can be squeezed down to a few nanometers, an interesting scale thus it fits well with the size of the targeted nano-object of interest.

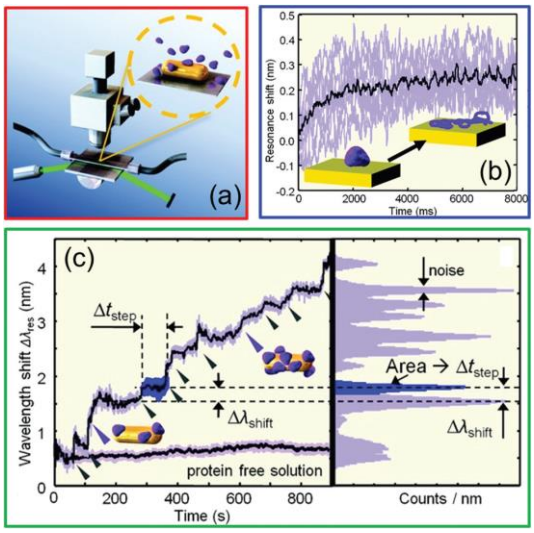

Figure 5 - Single molecule detection by taking advantage on the gold nanorods enhancement. Taken from [52]

The combination of WGM resonators and plasmonic nanostructures in hybrid plasmonic-photonic biosensors therefore seems particularly promising. The WGM component provides sharp resonances, which are an indispensable ingredient to monitor the binding of small objects (or, in other words, to maintain a very low detection limit). The plasmonic component provides a strong enhancement of the electromagnetic field, which improves the sensitivity of the device. Adsorption of the plasmonic structure causes a decrease in the Q-factor of the hybrid resonator to approximately 10^5–10^6, that is one/two orders of magnitude lower than the values reported for the bare WGM resonators (Table 2 in [50]).

First hybrid coupling of plasmonic and photonic modes has already been proposed, as in the case of photonic crystal cavities and metallic antennas [53], [54]. However the high-Q WGM resonators show unmatched sensitivity and several studies on hybrid plasmonic–photonic WGM resonators have already been conducted in the last few years [55]–[58].

In these cases micro-toroids and microspheres are used as photonic structures and are covered with metallic (gold) LSP nanostructures (nanoparticles [57], nanorods [59], nanoshells[55], [60], nanoprisms [61] and nanostars [62]). Different strategies can be used to induce the adsorption of nano-metallic objects on the surface of WGM resonators. For example, plasmonic nanoparticles

can be appropriately decorated with binders for the recognition of a specific analyte and for the chemical bond on the surface of the resonator. The latter is properly functionalized with aminosilanes to improve particle adhesion [63]. A different technique used involves the absorption of metal nanostructures on the surface of the WGM resonator by means of an acid solution. The evanescent field of the WGM mode circulating in the resonator exerts optical capture forces on the nano-metallic objects. When the pH of the solution in which they are suspended is sufficiently low (pH ~ 1.5), irreversible adsorption takes place[64].

Finally, in regards to integration with LSPR nanostructures, on-chip rings and microdisks pave the way for new perspectives with respect to other WGM families of structures. In fact, by implementing dedicated lithographic steps, LSPR structures can be integrated into the WGM cavity in a controlled manner and by following a top-down approach.

Another important issue when it comes to high performance hybrid WGM resonators, is to avoid quenching the resonance modes given by leakage in the metal. For this reason, a limited number of nanoparticles can be used, and, depending on the resonator morphology, the nanoparticles may need to be localized in a specific place. To meet these requirements, several methods have been developed to control the self-assembly of on chip integrated optoplasmonic resonators.

The study and investigation of these hybrid structures was more focused on the detection of biological nano-objects, such as a single bovine serum albumin (BSA) protein (mass: 66 kDa), a single RNA virus (MS2-virus, diameter: 27 nm), a really short oligonucleotide chain (8-mer, mass: 2.35 kDa), and a single tumor marker (thyroglobulin, mass: 660 kDa). Very recently, the kinetics and conformational dynamics of single enzymes have been evaluated by means of hybrid WGM resonators. An example of a typical approach is shown in Figure 6.a and b, with reference to the work done by Dantham and colleagues [65]. The spectral shifts measured at the time of binding on the resonant plasmonic structures are in the range of 1-30 fm, which are one to three orders of magnitude larger than the shifts measured for a bare photonic cavity with similar bound objects. In fact, the enhancement is further greater than expected by the principle of reactive detection. The reason is that the increase in the experimental field near the nano metal shell is higher than predicted by the theory, and this is due to the nano-roughness of the surface (nano-shell) which is clearly evident in the TEM images of the nano gold shell used (insert of Figure 6.b). The rationale is that the increase of the field near the nano metal shell is higher than predicted by the theory, and

this is due to the nano-roughness of the surface (nano-shell) which is clearly evident in the TEM images of the nano gold shell used (insert of Figure 6.b). The explanation is that the increase of the experimental field near the nano metal shell is higher than expected by the theory, and this is due to the nano-roughness of the surface (nano-shell) which is quite evident in the TEM images of the nano gold shell used (insert of Figure 6.b). The nanoroughness gives a further enhancement of the field in an extremely small nano-spot, whose dimensions are comparable to those of the proteins under examination (Figure 6.c and d). The main disadvantage when using a single LSPR structure linked to the WGM resonator is that while the volume of the optical mode is substantially the same as that of a WGM photonic resonator, the active detection area is reduced. To overcome this limitation, hybrid structures with multiple plasmonic structures positioned along the resonator equator are being investigated [56], [60], [64].

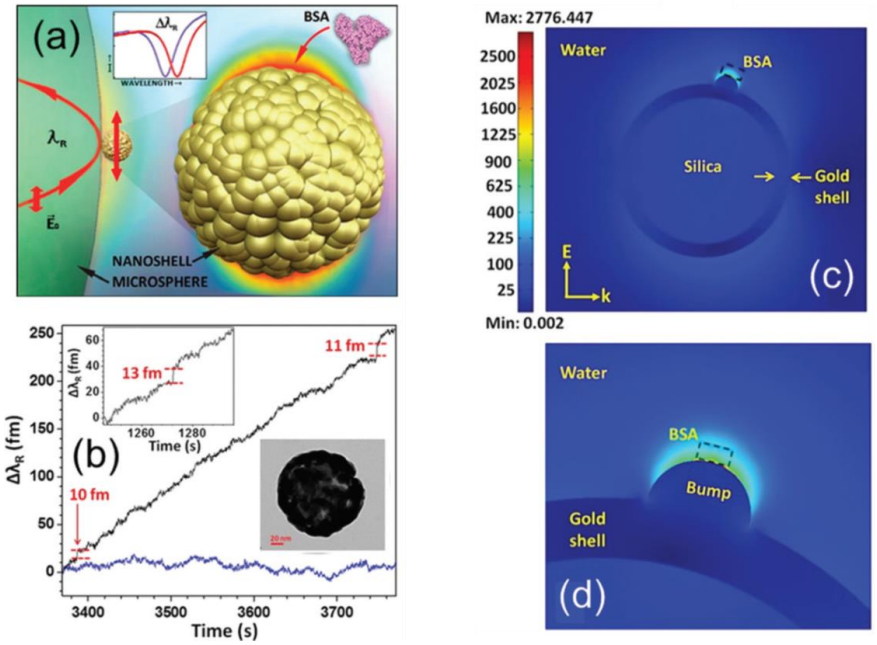

Figure 6 - Single particle detection with a hybrid plasmonic–photonic WGM resonator. Adapted from [66].

1.5 Slotted photonic structures

As it has been seen, the hybridization of photonic structures with plasmonic hot-spots determines a significant enhancement of the sensitive field, however it has the important drawback related to the volume of the mode. The limiting factor is given by the sensing method used, in fact the detection is carried out with the evanescent field that comes out of the resonant cavity. To increase

the sensitivity of the structure, it is necessary to operate on the overlap of the sensitive field with the particle that has to be detected. This section describes an approach developed to improve the accessibility to the sensing field through purely dielectric photonic structures: slotted ring resonators [67] and slotted photonic crystals [68]. The idea of the slotted-waveguide, two high-index waveguides separated by a thin low index region, has been introduced by Almeida et al. [69] and is based on TIR for strongly guiding and confining light to a low refractive index at the nanoscale.

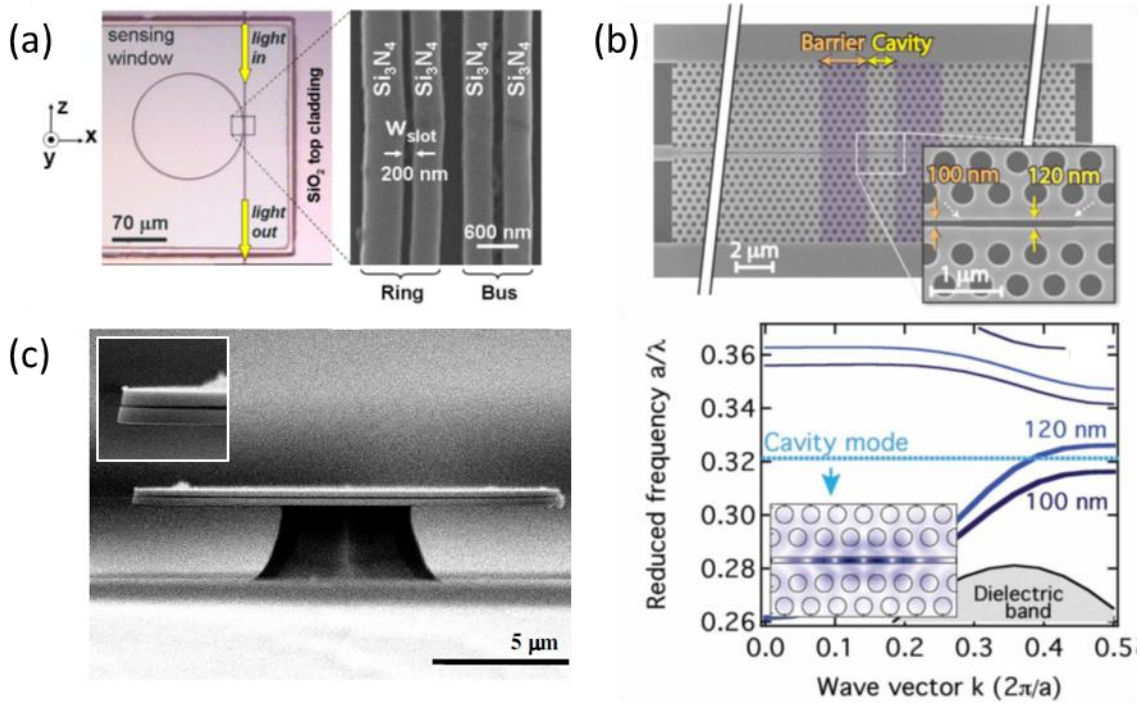

Figure 7 – (a) Silicon nitride slot ring resonator and slot waveguide. Taken from[70]. (b) SEM pictograph of the air-slot cavity. Theoretical dispersion curves of the air-slot cavity resonance (dashed lines) and the PhC slot waveguides (solid lines) are shown in the graph below, together with the electric field distribution of the cavity mode. Taken from [77]. (c) SEM pictograph of the horizontal air-slot resonator. Taken from [78]

A first example of SOI slot waveguides has been reported by Baehr-Jones et al. [73] which proposed oval resonator geometries with Q-factor up to 27 000. For ring resonators based on slot-waveguide on SOI structure, a refractive index sensitivity of 2×10^{-5} RIU with a small footprint is reported [72]. Examples of silicon nitride slot structure was then proposed by Barrios et al [74] with a detection limit of 2×10^{-4} RIU and a bulk sensitivity of 212 nm/RIU, and improved by Carlborg et al. [71]. In this case a detection limit of 0.9 pg/mm^2 has been reported for a packaged array of optical-slot-waveguide silicon nitride ring-resonator sensor, obtained as surface sensitive

detection [71]. Finally a SiN slot waveguide-based sensor was used by Taniguchi et al. to detect PSA (Prostate Specific Antigen) down to concentration of 10 ng/mL [75].

Slotted photonic crystals merge the temporal confinement provided by photonic crystalline cavities with the spatial confinement of the optical field provided by the slot waveguides. Example of sensitivity obtained with this approach is reported by Scullion et al. [68], where the detection of binding molecule is done in condition of low surface mass density. In another case, the slot photonic crystal geometry has been exploited by Di Falco et al. in a label-free biosensor, reaching a detection limit of 7.8×10^{-6} RIU with a quality factor up to *50000* [76]. Horizontal slot waveguide configuration were also proposed both in silicon and silicon nitride material [78]-[80]. Figure 7.c reports the structure reported by Lee et al. [78], consisting in an horizontal air-slot silicon nitride microring resonator, with a limit of detection of 30 ng/mL in biotin-streptavidin recognition and a quality factor of *7000* in the TM mode.

1.6 Pedestal waveguide

A different method to increase the overlap between the sensing field of the photonic structure and the analyte solution is that of using suspended or pedestal waveguides. By using resonators suspended on a pedestal, the active region acting as sensor is enlarged to the 3D domain. Since the use of suspended silicon waveguides was theoretically proposed in 2000 by Veldhuis et al. [81], different geometries have been exploited within this configuration. A sub-micron disk resonator of silicon suspended on a SiO_2 pedestal was proposed for optical sensing by Wang et al. [82], bulk sensitivity, tested in NaCl solution, was measured to be *130* nm/RIU. A more complex structure, with a sensitivity of *290* nm/RIU, was demonstrated by Hu et al. [83].

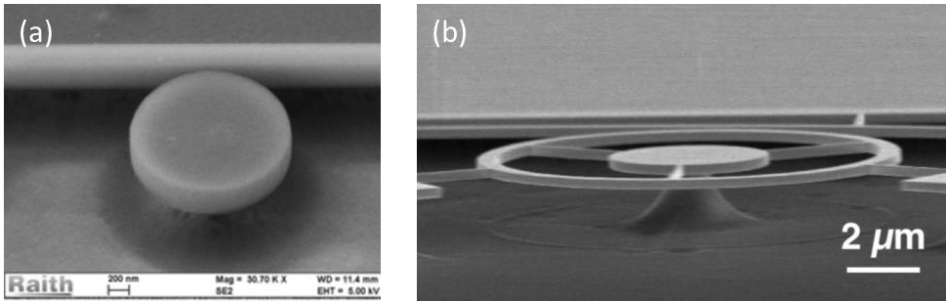

Figure 8 - (a) SEM pictograph of pedestal silicon microring resonator. Taken from [82]. (b) SEM pictograph of suspended microring resonator. Taken from [83]

[1] S. Dante, D. Duval, B. Sepulveda, A. B. González-Guerrero, J. R. Sendra, and L. M. Lechuga, "All-optical phase modulation for integrated interferometric biosensors," *Opt. Express*, vol. 20, no. 7, pp. 7195–7205, 2012.

[2] F. Prieto, B. Sepulveda, A. Llobera, C. Z. Vision, S. National, and L. M. Lechuga, "An integrated optical interferometric nanodevice based on silicon technology for biosensor applications," *Nanotechnology*, vol. 14, no. 2003, pp. 907–912, 2003.

[3] A. Ymeti *et al.*, "Fast, Ultrasensitive Virus Detection Using a Young Interferometer Sensor," *Nano Lett.*, vol. 7, no. 2, pp. 394–397, 2007.

[4] B. H. Schneider, J. G. Edwards, and N. F. Hartman, "Hartman interferometer: Versatile integrated optic sensor for label- free, real-time quantification of nucleic acids, proteins, and pathogens," *Clin. Chem.*, vol. 43, no. 9, pp. 1757–1763, 1997.

[5] M. J. Swann, L. L. Peel, S. Carrington, and N. J. Freeman, "Dual-polarization interferometry: An analytical technique to measure changes in protein structure in real time, to determine the stoichiometry of binding events, and to differentiate between specific and nonspecific interactions," *Anal. Biochem.*, vol. 329, no. 2, pp. 190–198, 2004.

[6] T. Hu, F. Yang, and X. R. Yang, "Real-time Study of Interaction Between Adenosine Triphosphate and Its Aptamer Using Dual Polarization Interferometry," *Chinese J. Anal. Chem.*, vol. 45, no. 7, pp. 944–950, 2017.

[7] J. Maldonado, A. B. González-Guerrero, C. Domínguez, and L. M. Lechuga, "Label-free bimodal waveguide immunosensor for rapid diagnosis of bacterial infections in cirrhotic patients," *Biosens. Bioelectron.*, vol. 85, pp. 310–316, 2016.

[8] C. S. Huertas, D. Fariña, and L. M. Lechuga, "Direct and Label-Free Quantification of Micro-RNA-181a at Attomolar Level in Complex Media Using a Nanophotonic Biosensor," *ACS Sensors*, vol. 1, no. 6, pp. 748–756, 2016.

[9] D. Dorfner *et al.*, "Photonic crystal nanostructures for optical biosensing applications," *Biosens. Bioelectron. J.*, vol. 24, pp. 3688–3692, 2009.

[10] H. Dutta, Sankar and S. Pal, "Design of a highly sensitive photonic crystal waveguide platform for refractive index based biosensing," *Opt Quant Electron*, vol. 45, pp. 907–917, 2013.

[11] G. Pitruzzello and T. F. Krauss, "Photonic crystal resonances for sensing and imaging Related content Photonic crystal resonances for sensing and imaging" *J. Opt.*, 20, 2018.

[12] P. M. Hui and N. F. Johnson, "Photonic Band-Gap Materials," *Solid State Phys.*, vol. 49, no. 1974, pp. 151–203, 1995.

[13] D. Biallo, A. D'Orazio, M. De Sario, V. Marrocco, V. Petruzzelli, and F. Prudenzano, "Photonic crystal sensors," *2006 Int. Conf. Transparent Opt. Networks*, vol. 2, no. July, pp. 44–48, 2006.

[14] M. J. Sweetman and N. H. Voelcker, "Chemically patterned porous silicon photonic crystals towards internally referenced organic vapour sensors," *RSC Adv.*, vol. 2, no. 11, pp. 4620–4622, 2012.

[15] C. J. Choi and B. T. Cunningham, “A 96-well microplate incorporating a replica molded microfluidic network integrated with photonic crystal biosensors for high throughput kinetic biomolecular interaction analysis,” *Lab Chip*, vol. 7, no. 5, pp. 550–556, 2007.

[16] A. Densmore *et al.*, “Spiral-path high-sensitivity silicon photonic wire molecular sensor with temperature-independent response,” *Opt. Lett.*, vol. 33, no. 6, pp. 596–598, 2008.

[17] Y. L. Vollmer F, “Label-free detection with high-Q microcavities: a review of biosensing mechanisms for integrated devices.,” *Nanophotonics*, vol. 1, no. 3–4, pp. 267–291, 2012.

[18] S. I. Shopova, R. Rajmangal, Y. Nishida, and S. Arnold, “Ultrasensitive nanoparticle detection using a portable whispering gallery mode biosensor driven by a periodically poled lithium-niobate frequency doubled distributed feedback laser,” *Rev. Sci. Instrum.*, vol. 81, no. 10, 2010.

[19] A. Ksendzov and Y. Lin, “Integrated optics ring-resonator sensors for protein detection,” *Opt. Lett.*, vol. 30, no. 24, p. 3344, 2005.

[20] M. Iqbal *et al.*, “Label-Free Biosensor Arrays Based on Silicon Ring Resonators and High-Speed Optical Scanning Instrumentation,” *IEEE J. Sel. Top. QUANTUM Electron.*, vol. 16, no. 3, pp. 654–661, 2010.

[21] I. M. White, H. Oveys, and X. Fan, “Liquid-core optical ring-resonator sensors,” *Opt. Lett.*, vol. 31, no. 9, p. 1319, 2006.

[22] T. Lu *et al.*, “High sensitivity nanoparticle detection using optical microcavities,” *Proc. Natl. Acad. Sci.*, vol. 108, no. 15, pp. 5976–5979, 2011.

[23] J. Su, A. F. G. Goldberg, and B. M. Stoltz, “Label-free detection of single nanoparticles and biological molecules using microtoroid optical resonators,” *Light Sci. Appl.*, vol. 5, pp. 1–7, 2016.

[24] A. Chiasera *et al.*, “Spherical whispering-gallery-mode microresonators,” *Laser Photonics Rev.*, vol. 4, no. 3, pp. 457–482, 2010.

[25] X. Fan, I. M. White, S. I. Shopova, H. Zhu, J. D. Suter, and Y. Sun, “Sensitive optical biosensors for unlabeled targets: A review,” *Anal. Chim. Acta*, vol. 620, no. 1–2, pp. 8–26, 2008.

[26] X. Lopez-Yglesias, J. M. Gamba, and R. C. Flagan, “The physics of extreme sensitivity in whispering gallery mode optical biosensors,” *J. Appl. Phys.*, vol. 111, no. 8, 2012.

[27] J. C. Knight, G. Cheung, F. Jacques, and T. A. Birks, “Phase-matched excitation of whispering-gallery-mode resonances by a fiber taper,” *Opt. Lett.*, vol. 22, no. 15, p. 1129, 1997.

[28] S. M. Spillane, T. J. Kippenberg, and K. J. Vahala, “Ultralow-threshold Raman laser using a spherical dielectric microcavity,” *Nature*, vol. 415, pp. 621–623, 2002.

[29] A. B. Petermann, A. Varkentin, B. Roth, U. Morgner, and M. Meinhardt-Wollweber, “All-polymer whispering gallery mode sensor system,” *Opt. Express*, vol. 24, no. 6, p. 6052, 2016.

[30] A. B. Petermann, M. Rezem, B. Roth, U. Morgner, and M. Meinhardt-Wollweber, “Surface-immobilized whispering gallery mode resonator spheres for optical sensing,”

Sensors Actuators, A Phys., vol. 252, pp. 82–88, 2016.

[31] D. K. Armani, T. J. Kippenberg, S. M. Spillane, and K. J. Vahala, "Ultra-high-Qtoroid microcavity on a chip," *Nature*, vol. 421, pp. 925–928, 2003.

[32] S. Feng, T. Lei, H. Chen, H. Cai, X. Luo, and A. W. Poon, "Silicon photonics: From a microresonator perspective," *Laser Photonics Rev.*, vol. 6, no. 2, pp. 145–177, 2012.

[33] M. Sumetsky, R. S. Windeler, Y. Dulashko, and X. Fan, "Optical liquid ring resonator sensor," *Opt. Express*, vol. 15, no. 22, p. 14376, 2007.

[34] H. Zhu, I. White, J. Suter, P. Dale, and X. Fan, "Analysis of biomolecule detection with optofluidic ring resonator sensors," *Opt. Express*, vol. 15, no. 15, p. 9139, 2007.

[35] I. M. White *et al.*, "Refractometric sensors for lab-on-a-chip based on optical ring resonators," *IEEE Sens. J.*, vol. 7, no. 1, pp. 28–34, 2007.

[36] J. T. Gohring, P. S. Dale, and X. Fan, "Detection of HER2 breast cancer biomarker using the opto-fluidic ring resonator biosensor," *Sensors Actuators, B Chem.*, vol. 146, no. 1, pp. 226–230, 2010.

[37] J. Wang, T. Zhan, G. Huang, P. K. Chu, and Y. Mei, "Optical microcavities with tubular geometry: Properties and applications," *Laser Photonics Rev.*, vol. 8, no. 4, pp. 521–547, 2014.

[38] W. Bogaerts *et al.*, "Silicon microring resonators," *Laser Photonics Rev.*, vol. 6, no. 1, pp. 47–73, 2012.

[39] L. Stefan, M. Bernard, R. Guider, G. Pucker, L. Pavesi, and M. Ghulinyan, "Ultra-high-Q thin-silicon nitride strip-loaded ring resonators," *Opt. Lett.*, vol. 40, no. 14, p. 3316, 2015.

[40] P. Dumon *et al.*, "Low-Loss SOI Photonic Wires and Ring Resonators Fabricated With Deep UV Lithography," *IEEE PHOTONICS Technol. Lett.*, vol. 16, no. 5, pp. 1328–1330, 2004.

[41] Q. Xu, B. Schmidt, S. Pradhan, and M. Lipson, "Micrometre-scale silicon electro-optic modulator," *Nature*, vol. 435, no. 7040, pp. 325–327, 2005.

[42] J. Schrauwen, S. Member, F. Van Laere, and S. Member, "Focused-Ion-Beam Fabrication of Slanted Grating Couplers in Silicon-on-Insulator Waveguides," *IEEE PHOTONICS Technol. Lett.*, vol. 19, no. 11, pp. 816–818, 2007.

[43] "Genalyte." [Online]. Available: www.genalyte.com. [Accessed: 12-Nov-2018].

[44] "Axela biosensors." .

[45] "Orphidia." [Online]. Available: http://www.orphidia.com/.

[46] E. Valera, W. W. Shia, and R. C. Bailey, "Development and validation of an immunosensor for monocyte chemotactic protein 1 using a silicon photonic microring resonator biosensing platform," *Clin. Biochem.*, vol. 49, no. 1, pp. 121–126, 2016.

[47] M. R. Foreman, J. D. Swaim, and F. Vollmer, "Whispering gallery mode sensors," *Adv. Opt. Photonics*, vol. 7, pp. 168–240, 2015.

[48] V. M. N. Passaro, B. Troia, M. La Notte, and F. De Leonardis, "Photonic resonant microcavities for chemical and biochemical sensing," *RSC Adv.*, vol. 3, no. 1, pp. 25–44,

2013.

[49] J. Su, “Label-Free Single Exosome Detection Using Frequency-Locked Microtoroid Optical Resonators,” *ACS Photonics*, vol. 2, no. 9, pp. 1241–1245, 2015.

[50] A. Bozzola, S. Perotto, and F. De Angelis, “Hybrid plasmonic-photonic whispering gallery mode resonators for sensing : A critical review,” *Analyst*, 2017.

[51] J. Zhu *et al.*, “On-chip single nanoparticle detection and sizing by mode splitting in an ultrahigh-Q microresonator,” *Nat. Photonics*, vol. 4, no. 1, pp. 46–49, 2010.

[52] I. Ament, J. Prasad, A. Henkel, S. Schmachtel, and C. Sönnichsen, “Single unlabeled protein detection on individual plasmonic nanoparticles,” *Nano Lett.*, vol. 12, no. 2, pp. 1092–1095, 2012.

[53] F. De Angelis *et al.*, “A hybrid plasmonic-photonic nanodevice for label-free detection of a few molecules,” *Nano Lett.*, vol. 8, no. 8, pp. 2321–2327, 2008.

[54] F. De Angelis *et al.*, “Nanoscale chemical mapping using three-dimensional adiabatic compression of surface plasmon polaritons,” *Nat. Nanotechnol.*, vol. 5, no. 1, pp. 67–72, 2010.

[55] S. I. Shopova, R. Rajmangal, S. Holler, and S. Arnold, “Plasmonic enhancement of a whispering-gallery-mode biosensor for single nanoparticle detection,” *Appl. Phys. Lett.*, vol. 98, no. 24, 2011.

[56] E. Arbabi, S. M. Kamali, S. Arnold, and L. L. Goddard, “Hybrid whispering gallery mode/plasmonic chain ring resonators for biosensing,” *Appl. Phys. Lett.*, vol. 105, no. 23, pp. 9–13, 2014.

[57] M. A. Santiago-Cordoba, S. V. Boriskina, F. Vollmer, and M. C. Demirel, “Nanoparticle-based protein detection by optical shift of a resonant microcavity,” *Appl. Phys. Lett.*, vol. 99, no. 073701, 2011.

[58] A. Kaplan *et al.*, “Finite element simulation of a perturbed axial-symmetric whispering-gallery mode and its use for intensity enhancement with a nanoparticle coupled to a microtoroid,” *Opt. Express*, vol. 21, no. 12, p. 14169, 2013.

[59] J. D. Swaim, J. Knittel, and W. P. Bowen, “Detection of nanoparticles with a frequency locked whispering gallery mode microresonator,” *Appl. Phys. Lett.*, vol. 102, no. 18, pp. 3–7, 2013.

[60] S. Arnold, V. R. Dantham, C. Barbre, B. A. Garetz, and X. Fan, “Periodic plasmonic enhancing epitopes on a whispering gallery mode biosensor,” *Opt. Express*, vol. 20, no. 24, p. 26147, 2012.

[61] H. Nadgaran and M. Afkhami Garaei, “Enhancement of a whispering gallery mode microtoroid resonator by plasmonic triangular gold nanoprism for label-free biosensor applications,” *J. Appl. Phys.*, vol. 118, no. 4, p. 043101, 2015.

[62] R. Guliaev, J. Xavier, and F. Vollmer, “Numerical analysis of plasmonic nanostar-whispering gallery mode hybrid microresonator,” *2017 Conf. Lasers Electro-Optics Eur. Eur. Quantum Electron. Conf.*, vol. 14169, no. 2013, pp. 1–1, 2017.

[63] S. Panich, K. A. Wilson, P. Nuttall, C. K. Wood, T. Albrecht, and J. B. Edel, “Label-free

Pb(II) whispering gallery mode sensing using self-assembled glutathione-modified gold nanoparticles on an optical microcavity," *Anal. Chem.*, vol. 86, no. 13, pp. 6299–6306, 2014.

[64] M. D. Baaske, M. R. Foreman, and F. Vollmer, "Single-molecule nucleic acid interactions monitored on a label-free microcavity biosensor platform.," *Nat. Nanotechnol.*, vol. 9, no. 11, pp. 933–9, 2014.

[65] V. R. Dantham, S. Holler, C. Barbre, D. Keng, V. Kolchenko, and S. Arnold, "Label-free detection of single protein using a nanoplasmonic-photonic hybrid microcavity," *Nano Lett.*, vol. 13, no. 7, pp. 3347–3351, 2013.

[66] S. Holler *et al.*, "The whispering gallery mode biosensor: label-free detection from virus to single protein," *SPIE Nanosci. + Eng.*, vol. 9166, p. 91660O, 2014.

[67] C. A. Barrios *et al.*, "Label-free optical biosensing with slot-waveguides," vol. 33, no. 7, pp. 708–710, 2008.

[68] M. G. Scullion, A. Di Falco, and T. F. Krauss, "Slotted photonic crystal cavities with integrated microfluidics for biosensing applications," *Biosens. Bioelectron.*, vol. 27, no. 1, pp. 101–105, 2011.

[69] V. R. Almeida, Q. Xu, C. A. Barrios, and M. Lipson, "Guiding and confining light in void nanostructure," vol. 29, no. 11, pp. 1209–1211, 2004.

[70] C. A. Barrios, "Optical Slot-Waveguide Based Biochemical Sensors," pp. 4751–4765, 2009.

[71] C. F. Carlborg, K. B. Gylfason, A. Kazmierczak, and F. Dortu, "A packaged optical slot-waveguide ring resonator sensor array for multiplex label-free assays in labs-on-chips," *Lab Chip*, vol. 10, no. 3, pp. 281–290, 2010.

[72] T. Claes, J. G. Molera, K. De Vos, E. Schacht, R. Baets, and P. Bienstman, "Label-free biosensing with a slot-waveguide-based ring resonator in silicon on insulator," *IEEE Photonics J.*, vol. 1, no. 3, pp. 197–204, 2009.

[73] T. Baehr-jones, M. Hochberg, C. Walker, and A. Scherer, "High-Q optical resonators in silicon-on- insulator-based slot waveguides," *Appl. Phys. Lett.*, vol. 081101, no. 86, pp. 6–9, 2005.

[74] C. A. Barrios *et al.*, "Slot-waveguide biochemical sensor," vol. 32, no. 21, pp. 3080–3082, 2007.

[75] T. Taniguchi, A. Hirowatari, T. Ikeda, M. Fukuyama, Y. Amemiya, A. Kuroda, S. Yokoyama, "Detection of antibody-antigen reaction by silicon nitride slot-ring biosensors using protein G," *Opt. Comm.*, vol. 365, pp. 16-23, 2016.

[76] A. Di Falco, L. O'Faolain, and T. F. Krauss, "Chemical sensing in slotted photonic crystal heterostructure cavities," *Appl. Phys. Lett.*, vol. 063503, no. 94, pp. 92–95, 2009.

[77] J. Jágerská, H. Zhang, Z. Diao, N. Le Thomas, and R. Houdré, "Refractive index sensing with an air-slot photonic crystal nanocavity," *Opt. Lett.*, vol. 35, no. 15, pp. 2523–2525, 2010.

[78] S. Lee, S. C. Eom, J. S. Chang, C. Huh, G. Y. Sung, and J. H. Shin, “Label-free optical biosensing using a horizontal air-slot SiNx microdisk resonator,” *Opt. Express*, vol. 18, no. 20, pp. 20638–20644, 2010.

[79] C. A. Barrios, “Ultrasensitive nanomechanical photonic sensor based on horizontal slot-waveguide resonator,” *IEEE Photonics Technology Letters*, vol. 18, no. 22, pp. 2419-2421, 2006.

[80] Kim, G.; Shin, J.H., “Luminescent silicon-rich nitride horizontal air-slot microdisk resonators for biosensing,” *IEEE Photonics Technol. Lett.*, vol. 28, pp. 2331–2334, 2016.

[81] G. J. Veldhuis, O. Parriaux, H. J. W. M. Hoekstra, and P. V Lambeck, “Sensitivity Enhancement in Evanescent Optical Waveguide Sensors,” *J. Light. Technol.*, vol. 18, no. 5, pp. 677–682, 2000.

[82] X. Wang, X. Guan, Q. Huang, J. Zheng, Y. Shi, and D. Dai, “Suspended ultra-small disk resonator on silicon for optical sensing,” *Opt. Lett.*, vol. 38, no. 24, pp. 5405–5408, 2013.

[83] S. Hu, K. Qin, I. I. Kravchenko, S. T. Retterer, and S. M. Weiss, “Suspended Micro-Ring Resonator for Enhanced Biomolecule Detection Sensitivity,” *Proc. SPIE*, vol. 8933, pp. 1–7, 2014.

Chapter 2
Modelling

Much time has passed since the first explanation of whispering gallery mode (WGM) phenomena by Lord Rayleigh around 1910 [1]. There has been an evolution from the observation of a similar process for electromagnetic waves in dielectric material [2] till their use in nonlinear optics field [3] and the first commercially available device with high-sensitivity and fast biosensing [4]. The first part of this chapter describes the basic theory and optical properties of WGM resonators, especially ring resonators. The second part, building upon the notions just described, introduces the photonic structure objective of this thesis and reports the development of the theoretical analysis from modelling. .

2.1 Basic Theory

Optical whispering gallery modes are due to the internal reflection of electromagnetic waves at the interface between resonator and external media. Within geometrical optics approximation, according to the Snell's law, the ray travelling in a dielectric resonator with a refractive index n_1, which is larger than the refractive index n_2 of the surrounding medium, impinges at the surface with an angle θ greater than the critical angle θ_C. This is confined into the cavity creating total internal reflection. After a complete roundtrip the electromagnetic waves overlap with each other causing constructive and destructive interference, leading to resonance and standing wave forms.

From the point of wave optics, the field profile inside the WGM resonator and the resonant frequencies can be approximated analytically only for high-symmetry configurations, such as for spherical or cylindrical resonators. For a first order approximation, the spectral position of the resonance in a rotational symmetric cavity with effective radius of the cavity mode R_{WGM} and effective refractive index of the guided mode n_{eff} is given by:

$$2\pi R_{WGM} = m\frac{\lambda_0}{n_{eff}} \tag{2.1}$$

Where m is an integer and λ_0 is the free space excitation wavelength. The equation simply states that the condition for resonance is achieved when the length of the roundtrip of the cavity is a multiple of the resonating wavelengths. Thus, by knowing n_{eff} it is often enough to estimate the spectral position of the resonances.

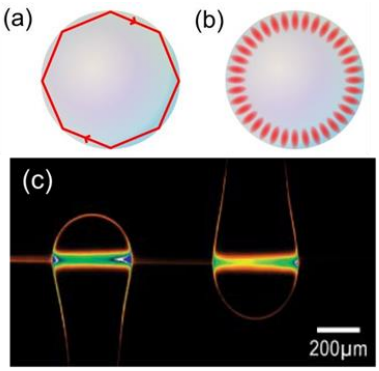

Figure 9 - Schematic representation of the resonating modes in optical cavities in (a) ray optics and (b) wave optics. (c) Optical picture of the standing wave profile in a resonant double sphere cavity system fed by a tapered optical fibre.[5]

When the system deviates from a perfect spherical or cylindrical symmetry, an analytical approach cannot be used anymore and numerical methods are necessary [6].

Although most of the field is confined in the resonator, a small fraction leaks out of the boundary of the cavity as an evanescent field. This evanescent tail is exploited for coupling light inside the cavity and plays a pivotal role in biosensing applications. Indeed, it can interact with the biomolecules that bind to the waveguide surface, or that flow over the resonator, and this will induce a variation in some of the resonator properties (resonance shift). This is known as reactive sensing principle (Figure 10.a); where the refractive index of the host medium changes due to the presence of an analyte, or when a particle/molecule attaches to the surface of the resonator. This changes the effective refractive index of the guided mode and this induces a redshift, $\Delta\lambda_r$, of the resonant frequency λ_r (from eq. 2.1). By monitoring this shift it is possible to detect the presence of the analyte, even in a quantitative way (Figure 10.b).

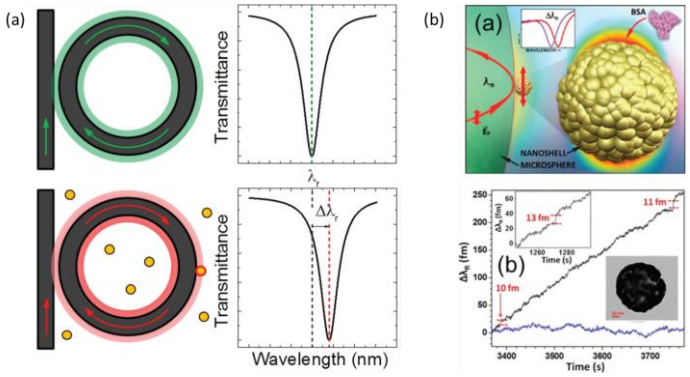

Figure 10 - (a) Reactive sensing principle and.(b) Single particle detection with hybrid photonic-plasmonic WGM resonator. Time-dependent resonance shift due to binding of BSA molecules. [7]

There are many different possible coupling schemes, for example prism coupling [8] and direct free-space coupling, but the most commonly used is coupling through fiber/waveguides in side coupling or grating configuration. In this scheme, referred to as "all-pass configuration", the resonances of the WGM cavity are typically monitored through the transmission spectrum. In the frequency domain, the transmitted power $\boldsymbol{P_{out}(\omega)}$ is typically Lorentzian [9]:

$$P_{out}(\omega) = P_0 \left[1 - K \frac{(FWHM/2)^2}{(\omega-\omega_0)^2+(FWHM/2)^2}\right] \tag{2.2}$$

Where $\boldsymbol{P_0}$ is the input power, $\boldsymbol{K}$ is the coupling coefficient, FWHM is the full-width at half-maximum, and $\boldsymbol{\omega_0}$ is the resonance frequency.

A typical transmission spectrum of a WGM structure (a silicon ring resonator) is reported in Figure 11, with all the relevant parameters. The coupling coefficient K determines how much light is coupled into the cavity. K=1 denotes the so-called critical coupling condition, where the light coupled to the resonant cavity equals the quantity of light lost during the roundtrip. Under this condition the transmission at resonance is $\boldsymbol{P_{out} = 0}$, thus it is the best condition to observe the mode resonances. As will be discussed later, a given cavity maximum field enhancement is achieved at this critical coupling condition.

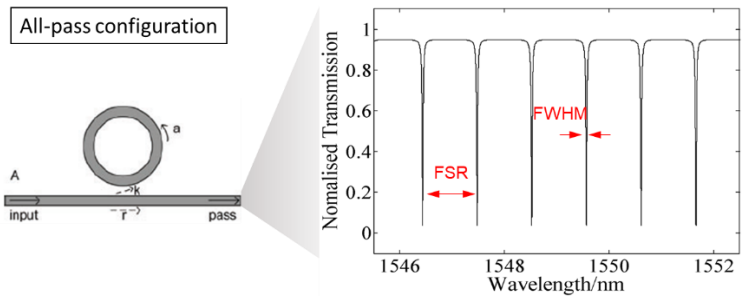

Figure 11 - Transmission spectrum of a classic WGM resonator. In particular for the case of a ring resonator in all-pass configuration.

2.2 Optical properties

2.2.1 Mode Volume

The mode volume indicates the spatial confinement of the resonating field inside the resonator, corresponding to the volume in which the main part of the modal energy is stored. It is a measure of how tightly light is confined in the cavity.

The mode volume V_m is defined as the ratio between the total energy within the region of interest and the maximum energy density [10]:

$$V_m = \frac{\int \varepsilon \cdot |E|^2 dv}{\varepsilon |E_{max}|^2} \tag{2.3}$$

Where ε is the permittivity of the medium, and where the integration is done over the whole cavity and the surrounding regions.

2.2.2 Free spectral Range

Free spectral range is the spectral distance between two adjacent modes. Since the modal structure of WGM resonators is quite complex and adjacent modes have generally different polarization and quantum numbers, it is only possible to approximate this definition by referring only to the azimuthal mode number *m*. The polarization, radial/axial mode numbers are kept fixed and the FSR is considered as the distance between modes *m* and *m+1*. Within this approximation, valid for $R \gg \lambda$, the free spectral range can be expressed as:

$$\delta\lambda_{FSR} = \frac{{\lambda_0}^2}{2\pi R n + \lambda_0} \approx \frac{{\lambda_0}^2}{2\pi R n} \tag{2.4}$$

So the free spectral range is the spectral distance between two consecutive resonances and depends on the size of the resonator. Large resonators are characterized by a very dense transmission spectrum while small resonators show widely spaced resonance peaks. The FSR directly affects the *dynamic range* of an optical sensor.

2.2.3 Finesse

Finesse (F) is defined as the ratio of the free spectral range and the width of the resonance for a specific wavelength, in terms of linewidth it can be written as:

$$F = \frac{\delta\lambda_{FSR}}{\Delta\lambda} \tag{2.5}$$

Hence it is an indicator of the spacing between adjacent resonances in comparison to their FWHM.

2.2.4 Quality factor

Quality factor is one of the most important parameters, representing the number of roundtrips that the resonating optical mode can make in the cavity and thus related to the effective interaction length between the sensing field and the particle.

More specifically it correlates the energy contained in the resonant structure with the energy lost through different loss mechanisms:

$$Q = \omega_0 \frac{U}{P_{loss}} = -\omega_0 \frac{U}{dU/dt} = \omega_0 \tau \tag{2.6}$$

Where U is the total energy stored in the cavity, ω_0 indicates the resonance frequency and P_{loss} is the total power loss of the cavity. As can be seen in eq. 2.6 the Q-factor is a measure of the temporal confinement of the energy inside the cavity. It relates to the time that a photon remains bound to the cavity before being lost in one of the different loss mechanisms, termed photon lifetime. It is also possible to write the photon lifetime as a function of the effective refractive index n_{eff} and of the loss coefficient, comprehensive of the overall losses, α:

$$\tau = \frac{n_{eff}}{c\alpha} \tag{2.7}$$

With *c* velocity of light in vacuum. Substituting this expression in eq. 2.6, the quality factor Q can be written as:

$$Q = \frac{\omega_0 n_{eff}}{c\alpha} \tag{2.8}$$

Finally the Q factor can be expressed in terms of resonance wavelength and full-width at half-maximum (FWHM), and thus can be directly and easily measured from the transmission spectrum. From eq 2.6, the total energy stored in the system decays as:

$$U \propto e^{-\omega_0 t/Q} \tag{2.9}$$

And thus the electric field inside the cavity vary as:

$$E(t) = E_0 e^{-\omega_0 t/2Q} e^{-i(\omega_0+\delta\omega)t} \tag{2.10}$$

Where $\delta\omega$ indicates the correction to the resonance frequency due to the losses. The spectral form of the resonance is given by a Fourier transform:

$$|E(t)|^2 \propto \frac{1}{(\omega-\omega_0-\delta\omega)^2+(\omega_0/2Q)^2} \tag{2.11}$$

This is a Lorentzian function with FWHM given by $\Delta\omega = \omega_0/Q$, thus:

$$Q = \frac{\omega_0}{\Delta\omega} = \frac{\lambda}{\Delta\lambda} = \frac{\lambda_{res}}{\text{FWHM}} \tag{2.12}$$

2.2.5 Field enhancement

The electric field enhancement can be estimated by the energy conservation of the system. If one considers a WGM cavity coupled to a bus waveguide, as in the case of ring resonator in all-pass configuration, the power flux brought to the cavity by the waveguide P_0 and the transmission coefficient T, then the energy flux coupled to the resonator can be expressed as:

$$P_0 \cdot (1 - T) \tag{2.13}$$

On the basis of the energy conservation principle, the energy dissipation rate into the cavity should be the same as the energy flux entering the same cavity, hence:

$$P \cdot \alpha \cdot L = P_0 \cdot (1 - T) \tag{2.14}$$

Where L is the length of the roundtrip and P is the power confined into the cavity. The field intensity enhancement can thus be obtained as the ratio of the power circulating in the cavity and the power "incident" on the cavity:

$$i_{En} = \frac{P}{P_0} = \frac{1-T}{\alpha \cdot L} \tag{2.15}$$

Finally, by substituting the eq. 2.8 the intensity enhancement can be written as:

$$i_{En} = \frac{cA_{eff}(1-T)}{\omega n_{eff}} \frac{Q}{V_m} \tag{2.16}$$

where $A_{eff} = V_m/L$ is the effective mode size.

The large field enhancement is given by a cavity with high Q-factor and small mode volume. Another parameter playing a role in field enhancement is the transmission coefficient T at the resonant wavelength. i_{En} is maximum for $T = 0$, that is in the condition of critical coupling; the internal losses of the cavity are equal to the coupling losses to the bus waveguide. Critical coupling is generally achieved by optimizing the distance between the input fiber / waveguide and the cavity surface, or by properly adjusting the width of the bus waveguide [11].

2.3 Loss Mechanisms

Loss mechanisms affecting photonic waveguides are mainly due to absorption of the guiding material, radiation and surface scattering. Assuming each mechanism as independent, the total power loss can be represented as the sum of the different contributions:

$$P_{tot} = \sum P_i \tag{2.17}$$

Thus the quality factor can also be split into different factors:

$$\frac{1}{Q_{tot}} = \sum \frac{1}{Q_i} \tag{2.18}$$

The higher the Q-factor of the loss mechanism, the less it contributes to the total Q-factor of the resonator.

2.3.1 Absorption losses

The absorption that an electromagnetic wave undergoes when travelling in a bulk material is expressed as the imaginary part of the refractive index of the material $n = n_r + in_i$ or in terms of absorption coefficient α:

$$I = I_0 e^{-\alpha x} \propto |E(x,t)|^2 \tag{2.19}$$

Using the definition of traveling plane wave:

$$E(x,t) = E_0 e^{i(kx-\omega t)} = E_0 e^{-\omega n_i x/c_0} e^{i\omega(n_r x/c_0 - t)} \tag{2.21}$$

The absorption coefficient can be written as:

$$\alpha = \frac{4\pi n_i}{\lambda_0} \tag{2.21}$$

In a time t, the light travels a distance $x = c_0 t/n_r$. Comparing eq. 2.8 and eq. 2.20, the quality factor related to the absorption losses can be expressed as:

$$Q_{abs} = \frac{2\pi n_r}{\alpha \lambda_0} = \frac{n_r}{2n_i} \tag{2.22}$$

The materials investigated and used in this work depend on the spectral range of interest. First modelling was carried out for silicon structure at the telecommunication wavelength. Secondly the visible range was investigated, thus different materials with low or no absorption at the resonating wavelengths were exploited, namely silicon nitride and silicon oxynitride.

2.3.2 Radiation losses

Radiation losses are due to the curvature of the cavity surface (*bending losses*) and to the presence of the coupling waveguide. For a given wavelength and radius, the number of energy density maxima is $2m$, thus the total energy stored in the resonator depends on the azimuthal mode number. Numerical simulations show that the Q-factor related to radiation losses Q_{rad} increase exponentially with m. It is shown that:

$$Q_{rad} \propto e^{2mh} \tag{2.23}$$

Where $h = \tanh(\sqrt{1 - 1/{n_{eff}}^2}) - \sqrt{1 - 1/{n_{eff}}^2}$. Since for a given wavelength the azimuthal mode number m scales proportionally to the cavity radius R, a similar dependence is assumed for Q_{rad} [30].

2.3.3 Scattering losses

The scattering loss mechanism is mainly determined by surface roughness and other imperfections, which are introduced during the fabrication process. This loss factor becomes more pronounced at shorter wavelengths, i.e. in the visible range. A further factor that causes an increase in scattering losses is the presence of metal nanoparticles linked to the surface of the cavity.

Fabrication processes have been deeply optimized over the years in order to reduce this unavoidable contribution, examples include resist reflowing [12], oxidation based smoothing [13]

and dry etching [14]. Concerning polymeric resonators, Q-factors between 10^4 and 10^6 have been achieved.

2.4 Modelling

Among the several structures described in the previous chapter, ring resonators have assumed a predominant role in the last few years due to their high Q-factor and the several advantages of their fabrication process. Indeed, planar ring resonators can be fabricated on a chip with processes already developed for micro and nano-electronics integrated circuit fabrication. This takes advantage of silicon photonics technology such as large-scalability and cost-effective production. In addition, several resonant structures and their bus waveguides can be patterned on the same chip, ensuring parallelization of the analysis and multiplexing.

In sensors development, an important parameter used to evaluate the sensor performance is the sensitivity. This is a measure of the efficiency of the biosensor, being the magnitude of the sensors' transduction signal differing due to the change in analyte conditions (quantity). Sensitivity is determined by the strength of light-matter interaction [15], [16]. In classical ring resonators, the spatial overlap is limited to the evanescent field at the surface of the structure, namely an exponential decaying field. Furthermore, the spectral shift is affected by the particle position with respect to the sensing mode; a small particle with a great overlap with the field can induce a shift similar to a larger particle with lower interaction with the mode. Thus the field distribution and particle position with respect to it play a fundamental role in particle detection.

We propose a novel design that allows enhanced sensitivity through a purely dielectric resonator, that is, without hybridization of the plasmonic nanostructures.

The structure modelled and investigated consists of a perforated silicon nitride ring resonator, namely a ring resonator standing on a dielectric substrate (SiO_2) and perforated by a subwavelength hole through the whole thickness to achieve the extreme overlap of the particles and the resonating mode. Innovative point of the proposed structure lies in the sub-wavelength hole that can also be seen as a point-like source for the electromagnetic field, highly confined in the tiny volume. A schematic of the structure is reported in Figure 12.

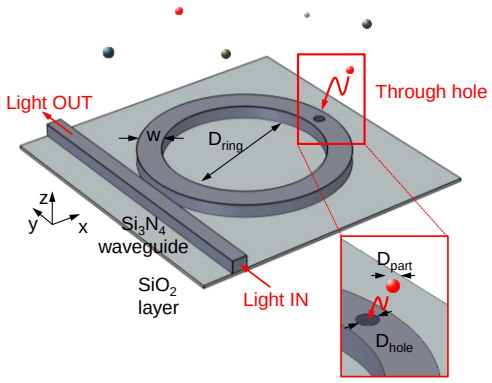

Figure 12 - Schematic of the designed novel structure. Ring resonator and dielectric waveguide are patterned on silica layers. The hole made in the ring allows the co-delivery of light and particles/molecules in solution inside the extremely confined space.

It is worth to note that the novel design studied can offer improvements both in current label-free detection methods and in the most diffused assays (fluorescence-based assays). Firstly, as further discussed in the next section, the hole induces a splitting of the resonating modes bringing some advantages to the classical sensing configuration. Secondly, the hole presents an extremely confined and uniform electromagnetic field within its cavity that can be exploited as a point-like source on-chip for background-free biosensors.

To validate the model, full 3D-FEM simulations were first performed considering a silicon ring (as in the most diffused platform of SOI) at the telecommunication wavelengths $1500 - 1600\ nm$. For the second step, a silicon nitride perforated ring resonator was investigated, to provide application in the visible-near infrared range.

A light source with a spatial shape as the fundamental TE mode is placed at the input port of the strip waveguide and classical parameters such as distance between the bus waveguide and the ring resonator, and the radius of the latter, are tested to find the most efficient structure. Later, an investigation of the effect of the insertion of the cylindrical cavity within the resonator on the split modes together with the dependence on the diameter of the hole was done. Finally, we looked at the application of the device as a biosensor, modelling the possibility for a higher number of holes in the resonator.

2.4.1 Defects and Mode Splitting

The effect of the nanometric size hole in the resonating structure is studied by performing three-dimensional FEM simulations. The splitting and optical properties of the cavity is studied as a function of the size of the hole and as a function of the number of holes.

WGM resonators supports degenerate modes, with the same resonant frequency and field distributions but opposite propagation directions, namely clockwise and counter-clockwise modes. If the resonator deviates from its perfect symmetry due to any kind of perturbation, this degeneracy is lifted to split in a doublet. Perturbation can be related to surface roughness, material inhomogeneity or a center of scattering, for example a particle/molecule bonded to the resonator surface. When the travelling mode encounters the defect the field is scattered elastically from the particle. Part of the light is scattered out from the structure and lost to the environment whilst another part is scattered back into the mode volume and starts propagating along the optical path of the counter-propagating frequency-degenerate mode. The portion of field lost to the environment can be seen as an additional damping factor while the coupling between the counter-propagating WGMs [17], [18] lifts the degeneracy of the two modes. The single resonance is split in a doublet structure, each related to the two new standing wave modes of the cavity. In the case of consecutive particle deposition, each absorbed particle causes the redistribution of the field modes in the cavity and thus will induce changes in the splitting and linewidth of the resonances.

A smart technique for using the resonators as a biosensor is presented by Zhu and coworkers [19], where the mode splitting phenomenon has been exploited, counting and sizing nanoparticles down to 30 nm in radius.

The same principle is used to model the effect of the insertion of the hole into the ring resonators, the hole can be treated as a scatterer and the light scattered by the hole are superposed coherently. Opportunely designed holes milled into the ring resonator cavity act as scatterers, inducing the mode splitting while limiting the losses to the environment and the subsequent damping of the energy stored in the resonator. The transmission spectrum of the bare ring resonator shows a single Lorentzian resonance for each resonant mode. The insertion of one hole into the resonating structure induces the formation of the standing wave modes (SWMs) and the Lorentzian peak splits into a doublet.

Figure 13 reports the simulated transmission spectra (for the fundamental TE mode) at the output port obtained for the conventional system. That is a standard ring resonator in an all-pass configuration, and the perforated ring. In panel b the splitting of the different modes is highlighted.

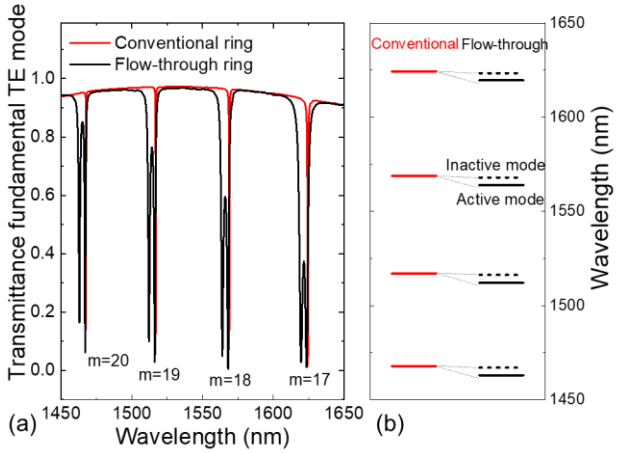

Figure 13 – (a) Transmission spectra for conventional ring (red) and through-hole ring (black). (b) Resonant wavelengths for the different configurations.

The FEM simulations led to interesting results concerning the field modes distribution inside the resonator. Indeed the degenerated modes are shifted so that the two have one maximum at the node and the other in the hole. This is the reason for the nomenclature adopted in Figure 13.b: active and inactive mode.

Looking more closely at specific resonances, the field profiles of the two degenerate modes appear clearly shifted, one with respect to the other, as can be seen in Figure 14. It is worth noting that the inclusion of the defect (the hole) also induces a widening of the resonance peak, thus reducing the quality factor.

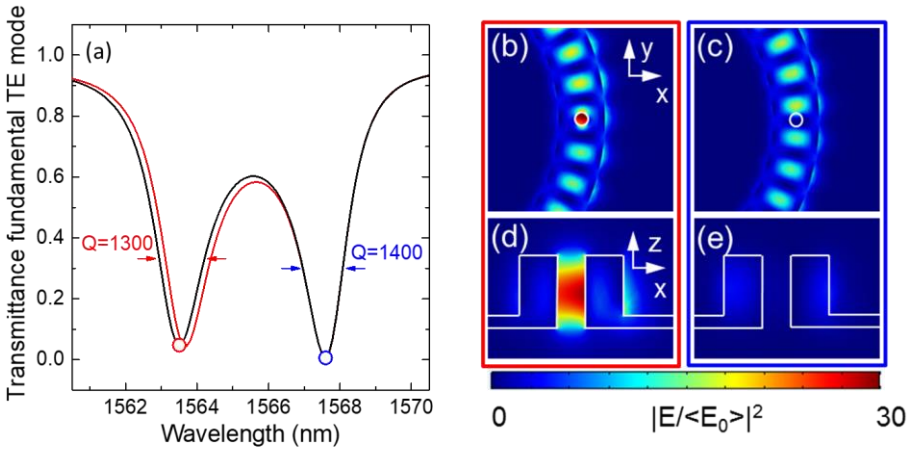

Figure 14 – (a) Transmission spectra of the TE fundamental mode for silicon through-hole ring of radius 3um and hole of 120nm. Red line indicate the spectral shift of the active mode due to a TiO_2 particle (n=2.4), while the blue peak is the resonance peak of the inactive mode. Top view of the field distribution of the active mode in the ring (b) and in the cross section at the hole (d). Top view of the field distribution of the inactive mode of the ring (c) and in the cross section at the hole (e).

The active mode is highly confined in the through-hole, thus it senses any variation of the refractive index inside the cavity (i.e. given by the passage of a nanoparticle). On the other hand the inactive mode remains buried in the resonator and experience no shift.

The profiles shown in Figure 14 relate to a silicon ring of diameter $3\ \mu m$ and hole of diameter $120\ nm$, the shift of the resonance of the active mode is due to the presence of a TiO particle (diameter $80\ nm$ refractive index $n = 2.4$). The uniformity of the field profile in the sensing hole is greatly improved compared to the other photonic crystal competitors.

2.4.2 Size of the Hole

According to the mode splitting theory, both the damping channel for scattering losses and the resonances' splitting vary with the diameter of the scatterer.

It is seen that a perfectly symmetric microresonator supports two counter-propagating modes with the same resonant frequency and field distributions but opposite propagation directions; clockwise (CW) and counter-clockwise (CCW) modes. In the presence of a scatterer, one of the two modes couples to it and scattered light couples back to either the CW or the CCW mode. This is valid whether the CW mode or the CCW mode couples to the scatterer and we can assume the same coupling coefficient g for these mechanisms. Indicating δ as the splitting of the modes, $\delta =$

$|\omega_1 - \omega_2|$, it is possible to express the coupling factor g as $2g = \delta$. The additional damping due to the scattering from the defect can be defined as Γ_R and can be seen in the transmittance spectrum as the broadening of the split modes, $\Gamma_R = \frac{1}{2}|\gamma_1 - \gamma_2|$, where γ_1 and γ_2 are the linewidths of the split modes.

From Hamiltonian description of the process, within the Rayleigh scattering condition, the coupling factor g and the damping parameter Γ_R are given by:

$$g = -\frac{\alpha f^2(r)\omega_c}{2V_c} \tag{2.24}$$

$$\Gamma_R = \frac{\alpha^2 f^2(r){\omega_c}^4}{6\pi v^3 V_c} \tag{2.25}$$

Where ω_c is the angular resonant frequency, $f(r)$ is the normalized mode distribution and V_c is the mode volume.

For a subwavelength scatterer, the interaction between the resonating modes and the scatterer can be modeled by using the dipole approximation [20] and can be related to the scatterer polarizability α.

The polarizability of an ellipsoid along the j-axis is given by [21]:

$$\alpha_j = 4\pi abc \frac{\varepsilon_1 - \varepsilon_m}{3\varepsilon_m + 3L_j(\varepsilon_1 - \varepsilon_m)} \tag{2.26}$$

With ε_1 component of the permittivity of the ellipsoid along the designated direction and ε_m permittivity of the medium and the with L_j depolarization factor along the j-axis:

$$L_j = \frac{1-e^2}{e^2}\left(-1 + \frac{1}{2e}\ln\frac{1+e}{1-e}\right) \tag{2.27}$$

and the eccentricity e:

$$e^2 = 1 - \frac{b^2}{a^2} \tag{2.28}$$

Approximating the scattering hole as a prolate spheroid (b=c) eq 2.26 can be written as:

$$\alpha_y = 4\pi abc \frac{\varepsilon_1 - \varepsilon_m}{3\varepsilon_m + 3L_y(\varepsilon_1 - \varepsilon_m)} \tag{2.29}$$

It is possible to simplify this to:

$$\alpha_y \sim \frac{4\pi ab^2}{3b^2} \frac{\varepsilon_1 - \varepsilon_m}{3\varepsilon_m + 3\left(\frac{b^2}{b^2-a^2}\right)(\varepsilon_1 - \varepsilon_m)} = \frac{4\pi a}{3} \frac{(\varepsilon_1 - \varepsilon_m)(b^2 - a^2)}{(b^2\varepsilon_1 - a^2\varepsilon_m)} \tag{2.30}$$

Approximating the ellipsoid to the scatterer it is possible to express the previous in terms of the hole radius R with $b = 2R$.

It is thus derived that the dependency of the coupling coefficient, and so the modes splitting, on the scatterers' dimensions.

3D-FEM simulations were used to model the effect exerted on the modes by holes of different sizes (Figure 15). In particular, the transmittance of the fundamental mode TE is observed for a hole with a diameter ranging from 50 nm to 300nm. From the derived spectra, information on the splitting of the modes and on the quality factor of the resonator are calculated.

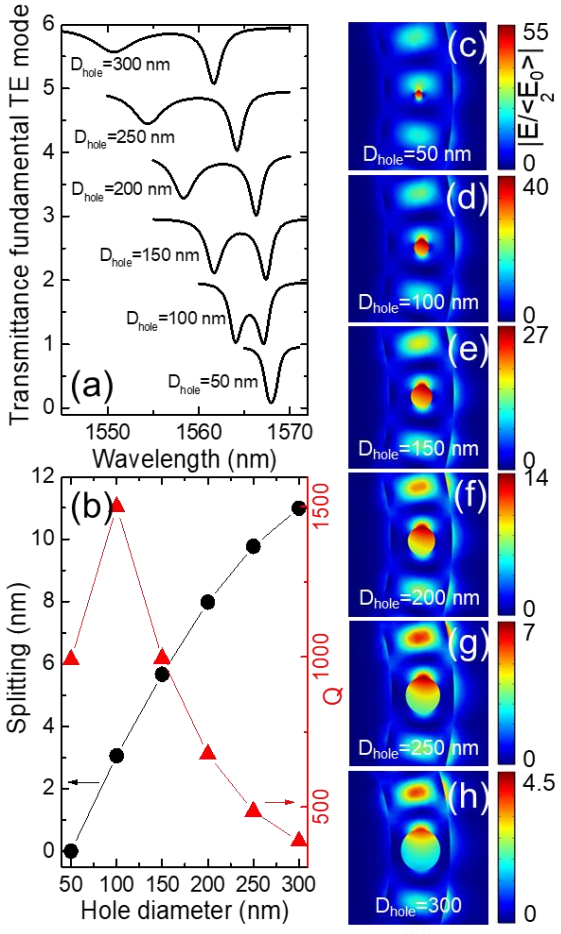

Figure 15 - Mode splitting dependence on the diameter of the hole. (a) Transmittance spectra for the fundamental TE mode. (b) Splitting of the modes and quality factor of the resonance peak of the active mode. (c) - (h) Fundamental TE mode distribution at the hole.

2.4.3 Waveguide Material

In integrated optics, SOI is the main exploited platform, operating at the telecommunication wavelengths around 1550 nm. An interesting alternative for Lab-On-a-Chip (LOC) biosensors is the shortwave near infrared (SW-NIR) region between 700 and 900 nm [22]. In particular, this is given by the use of biological samples. Indeed the easiest case is the detection of analytes dissolved in aqueous systems and the water absorption coefficient at these wavelengths is about 0.043 1/cm (0.19 dB/cm), three orders of magnitude lower than at 1550 nm [14].

To this purpose, the use of silicon oxynitride ($SiON_x$) waveguides [23] and Si_3N_4 waveguides [24] has been proposed from 2008 to 2011. Another advantage of the use of silicon nitride as a guiding material is due to its resistance to the diffusion of moisture and sodium ions, thus it can maintain a stable refractive index when operating in biological liquids.

As for the SOI structure, this waveguide technology is based on a combination of (stoichiometric) silicon nitride (SiN_x) Si_3N_4 as waveguide layers, deposited onto a buffer oxide layer. A further SiO_2 layer is deposited onto the photonic structures acting as a cladding layer. SiO_2 and Si_3N_4 layers are deposited by low-pressure chemical vapor deposition (LPCVD) and/or plasma enhanced chemical vapor deposition (PECVD). Thermal oxidation and atomic layer deposition (ALD) can also be used.

Moving from silicon to silicon nitride brings some variation to the constraints used and in the optical performance of the structures. In particular, there are two main variation with respect to the SOI case. Silicon nitride has lower refractive index with respect to silicon, thus the index contrast at the interface of the resonator is lower. From a modeling point of view this implies a major damping due to the bending losses. To keep a consistent field confinement and high Q-factor a possibility is to design resonators with a greater bending radius. A second cause of the lower quality factor is due to the wavelength range investigated. As already mentioned, shorter wavelengths are more sensitive to surface imperfections, thus scattering loss mechanisms assume higher importance. The constant improvements in the fabrication techniques help to obtain always more compact and better performing high-Q silicon nitride cavities.

3D-FEM simulations run for the silicon nitride resonator (Figure 16) show a broadening of the resonance mode peaks in the transmittance spectrum.

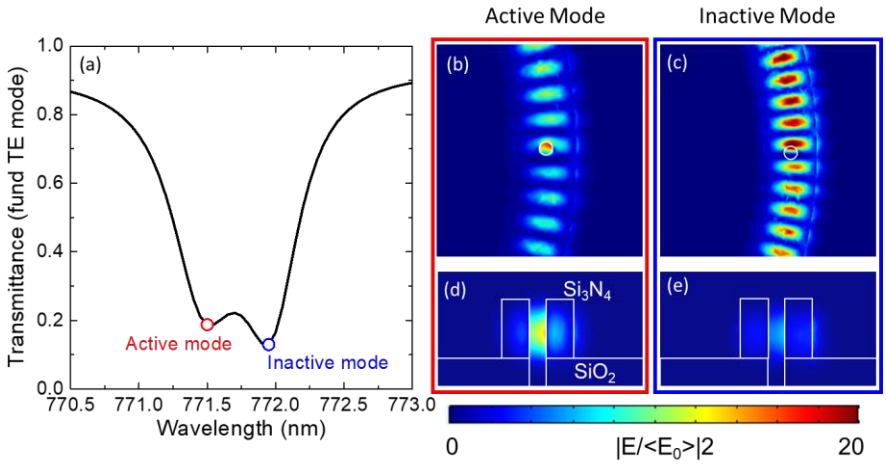

Figure 16 - (a) Transmission spectra of the TE fundamental mode for silicon nitride through-hole ring of radius 7um and hole of 120nm. Top view of the field distribution of the active mode in the ring (b) and in the cross section at the hole (d). Top view of the field distribution of the inactive mode of the ring (c) and in the cross section at the hole (e).

2.4.5 Multiple Holes

In analogy with the case of multiple particle adhesion on the WGM surface [19], the effect of multiple holes inside the ring resonator perimeter is investigated. Mode splitting properties using the coupled mode theory are discussed.

In the case of consecutive events, i.e. adsorption of particles onto the surface, each binding event induces a rearrangement of the resonating modes inside the WGM resonator. In the same way the distribution of the modes and thus the position and amplitude of the resonance peaks are strictly related to the number of holes inserted and their relative positions. Detailed theoretical analysis has been reported [25], where the case of a periodic distribution of holes in a dielectric ring to form a PhC resonator is considered.

We investigated also the effect of incrementing an even number of holes from 2 to 8 holes in symmetrical positions. The symmetrical disposition is chosen to maximize the probability of attaining a maximum of the field. Introducing one hole into the resonator acts as the border constraint of a Fabry-Pérot cavity, establishing the positions of the nodes into the resonant cavity where the CW and the CCW modes travel. Given the ring symmetry, by symmetrically positioning the additional holes would seem to be the most advantageous.

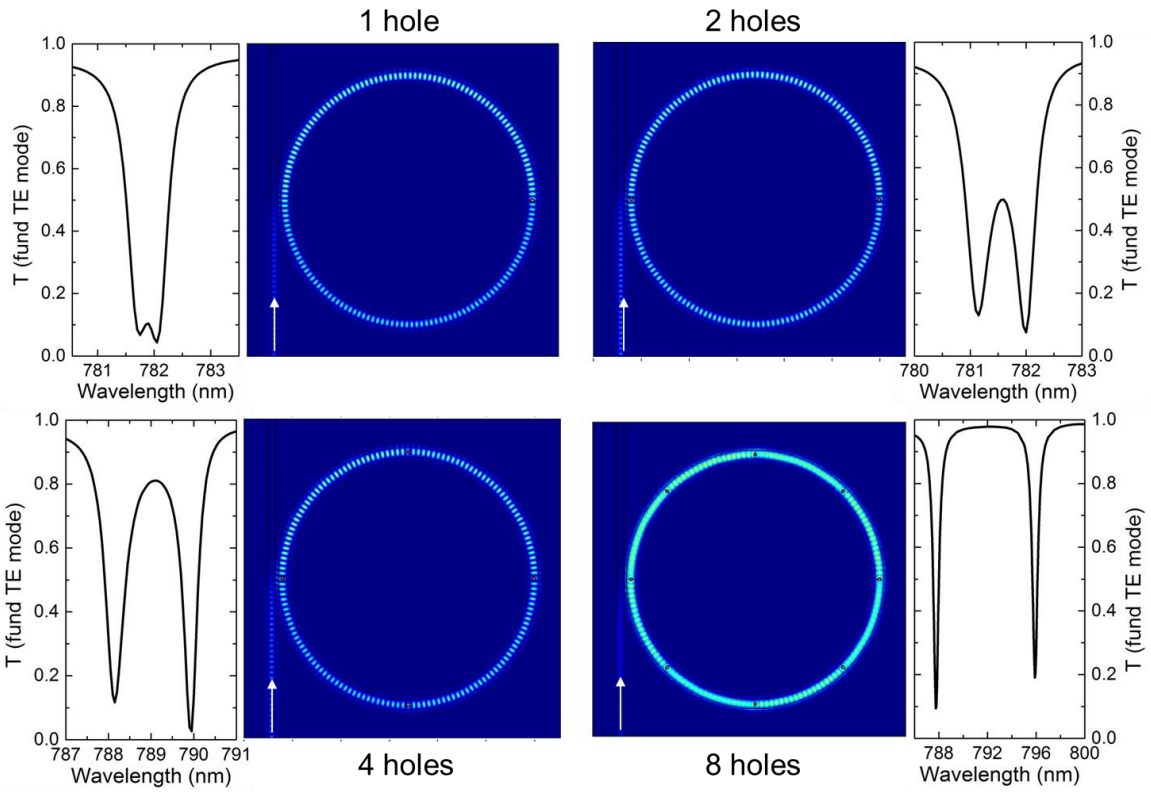

Figure 17 - Transmittance spectra of the TE fundamental mode and field distribution inside the resonator in case of multiple holes. Horizontal axis with different scale is used for each of the four cases.

As predicted from the theoretical model, introducing an increased number of holes (i.e. scatterers) increases the scattering losses factor with a consequent reduction of the quality factor of the resonator. With regard to the split modes' resolution, the broadening of the resonances is compensated by the increase in splitting.

As discussed previously, one of the most important aspects of the analyzed structure is the high field confinement inside the hole. This property is maintained in the case of multiple holes, as can be seen in Figure 18, where the field profile of the fundamental TE mode in a Si_3N_4 ring resonator with 4 through-holes is reported.

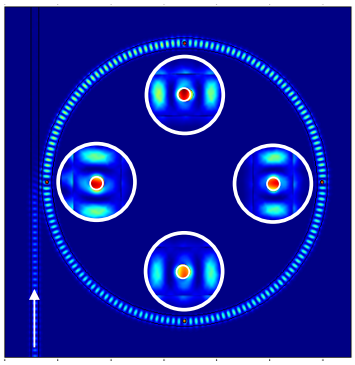

Figure 18 - Field profile of the fundamental TE mode in a Si_3N_4 ring resonator with 4 through-holes. Each white circle shows the magnification of the field in correspondence of the closest hole.

2.5 Sensitivity and Limit of Detection (LOD)

Sensing mechanisms generally used with resonator structures are based measuring the shift of the resonant wavelength due to the interaction between the analyte and the field mode of the resonator. From the reactive sensing principle applied to the case of a single particle or molecule [26], [27] the resonance redshift $\Delta\lambda_r$ can be indicated in terms of the particle polarizability α and of the magnitude of the electric field at the particle location ($E_0(r_p)$):

$$\frac{\Delta\lambda_r}{\lambda_r} = \frac{W_p}{W_c} = \frac{\alpha E_0(\mathbf{r}_p)^2}{2\int \varepsilon(\mathbf{r}_c) E_0(\mathbf{r}_c)^2 dV_c}, \tag{2.31}$$

Where W_c is the energy (averaged over one optical cycle) stored in the WGM cavity ($W_c = \frac{1}{2}\int \varepsilon(r_c)\alpha E_0(r_c)^2 dV_c$), W_p indicate the analogous work required to polarize the particle ($W_p = \alpha E_0(r_p)^2/4$), and ε is the permittivity of the resonator material.

For a conventional WGM cavity, $E_0(r_p)$ is simply the value of the evanescent tail of field at the surface of the resonator. For the perforated hole, the electric field at the particle location ($E_0(r_p)$) coincides with the highly confined mode into the through-hole.

Sensitivity can also be expressed as the change in resonance wavelength per change in the refractive index unit:

$$S = \frac{\Delta\lambda_{res}}{\Delta n_{eff}} \tag{2.32}$$

The sensitivity of the model studied, with the case of a single hole in a ring resonator of radius *3 μm*, is significantly enhanced with respect to a "classical" ring resonator of the same size and material. The 3D-FEM simulations performed led to the estimation of an improvement of almost one order of magnitude. The colour plots collected in Figure 19 report the sensitivity of the two systems as a function of the size and refractive index of the particle sensed. Enhanced sensitivity is expected as a consequence of the greater overlap of the particle and the resonating mode.

In Figure 19, the detection limit is also indicated, the LOD is a fundamental parameter when dealing with biosensors. This is the measurement of the minimum number of particles or molecules (or proteins) that can be detected after binding on the surface of the sensor. This quantitative result is fundamental when comparing different structures available or designed.

LOD of a WGM resonator depends on the sensitivity of the system and on the FWHM (or Q-factor) of the resonant mode. It is commonly assumed that shifts of the order of 1/1000 – 1/100 of the *FWHM* can be detected with an adequate signal-to-noise ratio [28], [29]. The analysis carried out assumes $\boldsymbol{\Delta\lambda_{res} = FWHM/100}$ as the minimum detectable shift. It is then possible to compare the sensors directly in terms of LOD:

$$LOD = \frac{FWHM/100}{S} = \frac{\lambda_{res}/100}{QS} \tag{2.33}$$

In the case of perforated ring resonators, the reduction of the Q-factor affects the important improvement in sensitivity.

The shift induced by a nanoparticle is very small and it is sensitive to the laser intensity and frequency fluctuations, thermal noise, detector noise and environmental disturbances. Analyzing the shift of the resonance active mode normalized to the un-shifted resonance peak would eliminate the noise affecting this measurement. This technique can thus be seen as a background-free single particle detection method.

In conclusion, the results related to the performance of the perforated ring resonator compared to the classic configuration are not of univocal interpretation. In general, it can be seen that the greater overlap of the field with the detected particle induces a spectral shift significantly greater than in the standard case. Considering a particle with a refractive index of *3* and a diameter of *70 nm*, there is a shift of about *200 nm* in the case of perforated rings compared to *30 nm* in the classic case. On the other hand, however, the structure is affected by the presence of the defect and the quality

factor is lower. Although the shift is greater, the observed peaks you are looking at are less sharp and therefore less easy to resolve. Overall, therefore, the LOD does not seem significantly better than the current state-of-the-art structures. From a practical point of view, however, the need to measure a higher shift implies the possibility of using less sophisticated analysis tools, impacting on the cost of the instrumentation.

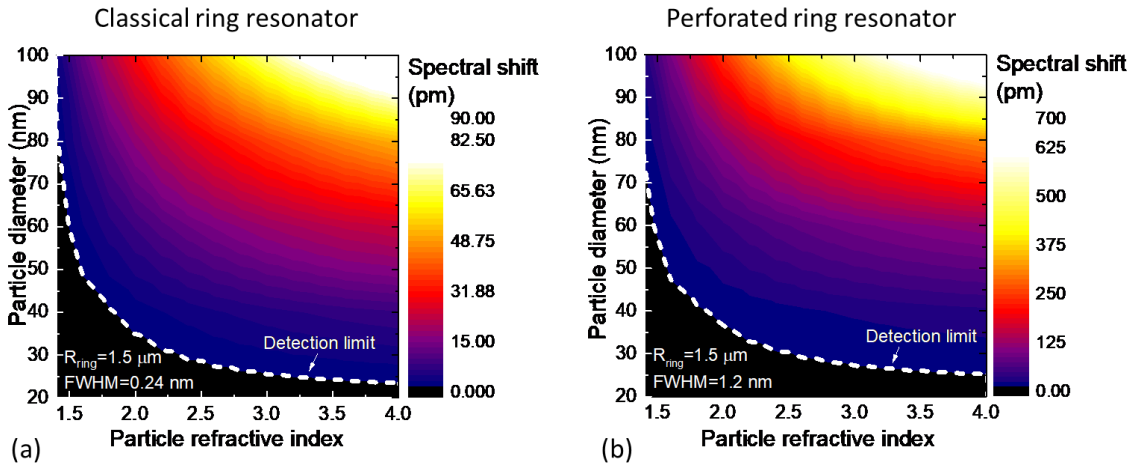

Figure 19 - Detection capability of a dielectric nanoparticle. Comparison of classical and perforated microring resonators. (a) Color plot of the spectral shift of the resonance when a nanoparticle for different radius and refractive index is attached to the outer side wall of a conventional ring resonator, in the position of maximum overlap with the evanescent field. (b) Color plot of the spectral shift of the active mode resonance when a nanoparticle for different radius and refractive index enter the hole of a perforated resonator. In both cases the ring diameter is 3 µm, and the modal volume is the same. The white dotted line indicates the detection limit (measurable minimum displacement of FWHM/100), and is found along a hyperbole.

[1] L. Rayleigh, “The problem of the whispering gallery,” *Philos. Mag*, vol. 20, pp. 1001–1004, 1910.

[2] R. D. Richtmyer, “Dielectric resonators,” *J. Appl. Phys.*, vol. 10, no. 6, pp. 391–398, 1939.

[3] D. Venkatakrishnarao, E. A. Mamonov, T. V. Murzina, and R. Chandrasekar, “Advanced Organic and Polymer Whispering-Gallery-Mode Microresonators for Enhanced Nonlinear Optical Light,” *Adv. Opt. Mater.*, vol. 6, no. 18, pp. 1–22, 2018.

[4] “https://www.genalyte.com/.” .

[5] F. Vollmer, S. Arnold, D. Braun, I. Teraoka, and A. Libchaber, “Multiplexed DNA quantification by spectroscopic shift of two microsphere cavities,” *Biophys. J.*, vol. 85, no. 3, pp. 1974–9, 2003.

[6] A. V Boriskin, S. V Boriskina, A. Rolland, R. Sauleau, and A. I. Nosich, “Test of the FDTD accuracy in the analysis of the scattering resonances associated with high-Q whispering-gallery modes of a circular cylinder,” *J. Opt. Soc. Am. A*, vol. 25, no. 5, pp. 1169–1173, 2008.

[7] V. R. Dantham, S. Holler, C. Barbre, D. Keng, V. Kolchenko, and S. Arnold, “Label-free detection of single protein using a nanoplasmonic-photonic hybrid microcavity,” *Nano Lett.*, vol. 13, no. 7, pp. 3347–3351, 2013.

[8] M. D. Baaske, M. R. Foreman, and F. Vollmer, “Single-molecule nucleic acid interactions monitored on a label-free microcavity biosensor platform.,” *Nat. Nanotechnol.*, vol. 9, no. 11, pp. 933–9, 2014.

[9] M. R. Foreman, J. D. Swaim, and F. Vollmer, “Whispering gallery mode sensors,” *Adv. Opt. Photonics*, vol. 7, pp. 168–240, 2015.

[10] I. H. Agha, J. E. Sharping, M. A. Foster, and A. L. Gaeta, “Optimal sizes of silica microspheres for linear and nonlinear optical interactions,” *Appl. Phys. B Lasers Opt.*, vol. 83, no. 2, pp. 303–309, 2006.

[11] J. Niehusmann, A. Vörckel, P. Haring Bolivar, T. Wahlbrink, W. Henschel, and H. Kurz, “Ultrahigh-quality-factor silicon-on-insulator microring resonator,” *Opt. Express*, vol. 20, no. 7, pp. 7526–7543, 2012.

[12] M. Borselli, T. J. Johnson, and O. Painter, “Beyond the Rayleigh scattering limit in high-Q silicon microdisks: theory and experiment,” *Opt. Express*, vol. 13, no. 5, p. 1515, 2005.

[13] K. K. Lee, D. R. Lim, L. C. Kimerling, J. Shin, and F. Cerrina, “Fabrication of ultralow-loss Si/SiO2 waveguides by roughness reduction,” *Opt. Lett.*, vol. 26, no. 23, p. 1888, 2001.

[14] S. Cheemalapati, M. Ladanov, J. Winskas, and A. Pyayt, “Optimization of dry etching parameters for fabrication of polysilicon waveguides with smooth sidewall using a capacitively coupled plasma reactor,” *Appl. Opt.*, vol. 53, no. 25, p. 5745, 2014.

[15] N. A. Mortensen, S. Xiao, and J. Pedersen, “Liquid-infiltrated photonic crystals: Enhanced light-matter interactions for lab-on-a-chip applications,” *Microfluid. Nanofluidics*, vol. 4, no. 1–2, pp. 117–127, 2008.

[16] I. M. White and X. Fan, “On the performance quantification of resonant refractive index sensors Ian,” *Opt. Express*, vol. 16, no. 2, pp. 1020–1028, 2008.

[17] T. J. Kippenberg, S. M. Spillane, and K. J. Vahala, “Modal coupling in traveling-wave resonators,” *Opt. Lett.*, vol. 27, no. 19, p. 1669, 2002.

[18] A. Mazzei, S. Gotzinger, L. de S. Menezes, G. Zumofen, O. Benson, and V. Sandoghdar, “Controlled Coupling of Counterpropagating Whispering-Gallery Modes by a Single Rayleigh Scatterer: A Classical Problem in a Quantum Optical Light,” *Phys. Rev. Lett.*, vol. 99, no. 173603, pp. 1–4, 2007.

[19] J. Zhu *et al.*, “On-chip single nanoparticle detection and sizing by mode splitting in an ultrahigh-Q microresonator,” *Nat. Photonics*, vol. 4, no. 1, pp. 46–49, 2010.

[20] D. Jackson, *Classical Electrodynamics*. New York: Wiley and Sons, 1962.

[21] C. F. Bohren and D. R. Huffman, *Absorption and scattering of light by small particles*. 1983.

[22] M. A. Cooper, *Label-free biosensors : techniques and applications*. Cambridge: Cambridge University Press, 2009.

[23] K. Wörhoff, E. Klein, G. Hussein, and A. Driessen, “Silicon oxynitride based photonics,” *Proc. 2008 10th Anniv. Int. Conf. Transparent Opt. Networks, Ict.*, vol. 3, pp. 266–269, 2008.

[24] J. F. Bauters *et al.*, “Ultra-low-loss high-aspect-ratio Si3N4 waveguides,” *Opt. Express*, vol. 19, no. 4, p. 3163, 2011.

[25] P. Xia, Y. Fu, M. Kong, Z. Liu, J. Zhou, and J. Zhou, “Theoretical Analysis of the Mode Splitting Properties in Periodically Patterned Microring Resonators,” *J. Light. Technol.*, vol. 35, no. 9, pp. 1700–1704, 2017.

[26] E. Arbabi, S. M. Kamali, S. Arnold, and L. L. Goddard, “Hybrid whispering gallery mode/plasmonic chain ring resonators for biosensing,” *Appl. Phys. Lett.*, vol. 105, no. 23, pp. 9–13, 2014.

[27] S. I. Shopova, R. Rajmangal, S. Holler, and S. Arnold, “Plasmonic enhancement of a whispering-gallery-mode biosensor for single nanoparticle detection,” *Appl. Phys. Lett.*, vol. 98, no. 24, 2011.

[28] I. Ament, J. Prasad, A. Henkel, S. Schmachtel, and C. Sönnichsen, “Single unlabeled protein detection on individual plasmonic nanoparticles,” *Nano Lett.*, vol. 12, no. 2, pp. 1092–1095, 2012.

[29] F. Vollmer and S. Arnold, “Whispering-gallery-mode biosensing: Label-free detection down to single molecules,” *Nat. Methods*, vol. 5, no. 7, pp. 591–596, 2008.

[30] S.L. McCall, A.F. J. Levi, R. E. Slusher, S.J. Pearton, R. A. Logan, “Whispering-gallery mode microdisk lasers,” *Appl. Phys. Lett.*, vol. 60, no. 3, pp. 289-291, 1992

Chapter 3
Optical characterization

This chapter reports the optical characterization of the perforated ring resonator. The first part is dedicated to the description of the structure of the chip and the fabrication process, followed by illustration of the optical setup adopted and the system used. In the second part, the optical characterization carried out is presented. We propose to characterize the designed platform. In particular, we want to characterize the element of novelty, which is the hole made inside the resonator. The key point of the system is that the hole can be assimilated to a point-like source, characterized by the modes of the resonant cavity. A sensing device based on the perforated ring will have a high signal-to-background-ratio, where the background is intended as the scattering losses from the waveguide and resonating structure.

3.1 Fabrication process and device description

3.1.1 Classic device

The fabrication process of dielectric waveguide and ring resonator have been investigated.

The general process can be summarized in four steps, schematically shown in Figure 20. On a polished silicon wafer are deposited *via* PECVD or LPCVD a layer of oxide (SiO_2) and a layer of guiding material. As for the SOI structure, the oxide layer serves to isolate the photonic system from the silicon substrate, preventing the losses due to coupling of the light travelling into the waveguides with the silicon substrate. The upper layer will constitute the photonic system, the choice of material is therefore mainly related to the wavelength range in which one wants to work. The technique of deposition of the latter may vary depending on the material deposited and the thickness of the layer.

The second step involves the definition of the waveguide using lithographic techniques such as EBL or Deep-UV lithography (193nm laser). Specifically, the resist is deposited by spin coating, follows patterning by electronic or optical lithography and final development. Depending on the

resist used, additional steps may be required. In case of positive resist (panel b1) at the development step will follow metal layer deposition and subsequent lift-off in acetone (or PG Remover) in order to have a metal mask. Regarding the metal deposition, e-beam evaporation is preferred to the faster sputtering techniques for its verticality, which leaves the vertical walls of the pattern free, thus easily accessible for the solvent, facilitating the lift-off. In case of negative resist (panel b2), the final pattern is directly obtained with the lithographic step. Although the latter assures a faster process, the first approach is generally preferred due to the greater ease of use. The negative resist is particularly sensitive to the preparation conditions, for example the baking temperature and the time between spin coating and exposure. This makes the process critical compared to the positive version, and therefore less used. However, this process also offers several advantages, in particular it allows to speed up and simplify the fabrication process, bypassing the evaporation and lift-off steps. Secondly, the use of a polymer mask instead of a metal one is suitable for a reduced lateral roughness of the guides and for possible dielectric-metal contaminations [1]–[3].

The resulting mask is then transferred to the photonic material by dry etching (Reactive Ion Etching, RIE) [4], [5], before being removed from the substrate by wet-etching.

Finally, an oxide layer is deposited on the system of waveguides, which serves to shield the inactive sensor region from the environment and helps to reduce scattering losses from the surface and protect covered (panel c). A last step consists in the definition of the active region of the sensor, resulting in an open window in the upper oxide-layer, in coincidence with the specific portion of the guide system used for sensing.

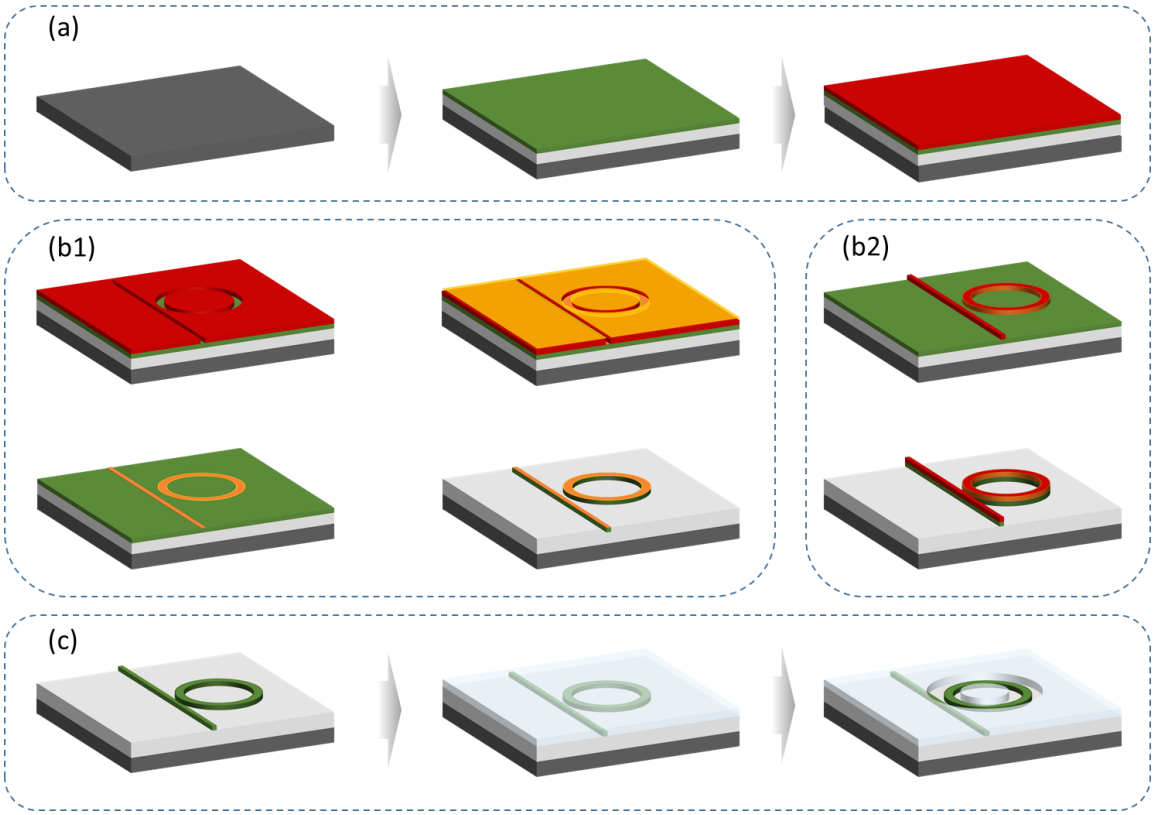

Figure 20 – General fabrication process. (a) On the silicon wafer are deposited oxide isolating layer and dielectric guiding material. Resist is finally spin coated on the substrate. (b1) Positive resist process version. After exposure and development a metal layer is deposited by vertical evaporation (up-right). Lift-off of the resist leaves the metal mask (low-left) and the pattern is transferred to the dielectric layer via dry-etching. Finally the metal mask is removed via wet-etch. (b2) Negative resist process version. The exposed resist is developed. The mask is transferred by dry-etching. (c) A layer of oxide material is deposited to protect the waveguides thus a window is opened by wet-etching to allow the resonator to sense the external media variation.

The device used to experimentally validate the modeled structure consists in SiON waveguides and resonators deposited onto *4 μm* thick SiO_2 layer. In particular, SiON waveguides of *380 nm* thickness and *900 nm* width are used to excite the resonating structure of a racetrack resonator of *100 μm* radius with *40 μm* coupling length. It should be noted that, within certain limits, lengthening the coupling section between the waveguide and the resonant structure, thus moving from the ring to the racetrack, results in better coupling efficiency.

The system of waveguides is covered by a TEOS layer of thickness 1 *μm*. The sensing region is determined by a window opened into this covering layer. This is obtained by wet etching in hydrofluoric acid solution (BHF 7:1), the mask used in this step is a patterned photoresist (Shipley S1813 Microposit).

A schematic illustration of the photonic integrated system and the cross section of the substrate are shown in Figure 21, together with SEM pictograph of the resonator.

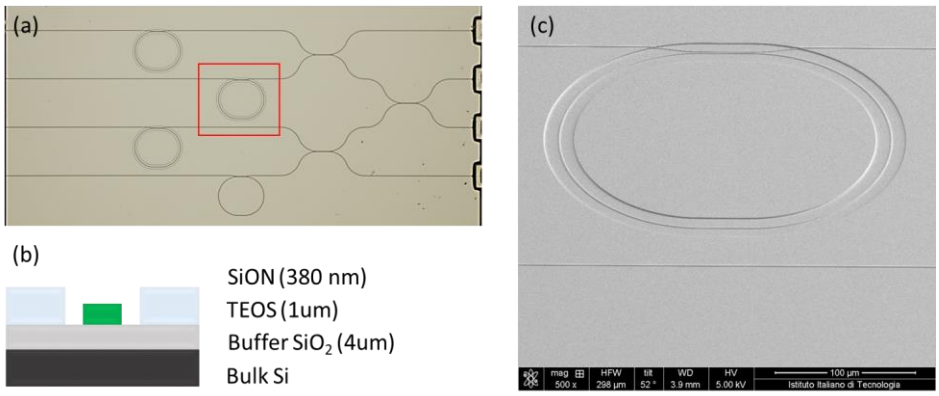

Figure 21 - On-chip photonic waveguides and resonators. (a) Optical image of the final chip. (b) Cross section with the different materials of the substrate. (c) SEM pictograph of the exposed racetrack.

3.1.2 Novelty

The novelty of the system studied lies in the sub-wavelength hole in the resonant structure. During this design and characterization stage, the hole is made in a second processing phase, i.e. on a "classic" photonic structure finished (figure 22). However, this change can be introduced into the current production process by simply making a modification in the mask design.

Sub-wavelength holes are made in the SiON resonator by Focused Ion Beam (FIB) milling. In particular the use of the dual-beam system (FEI Helios Nanolab 600), gives the possibility of aligning the pattern through SEM imaging minimizing the use of ion beam scan. This is essential as it avoids damaging the surface of the waveguide by introducing scattering elements that would reduce its optical qualities. Holes of different diameter have been tested, with a diameter varying from *50 nm* to *370 nm*.

After the milling of the holes, the surface is passivated with *2 nm* of SiO_2 deposited by Atomic Layer Deposition (ALD). ALD deposits a uniform layer conformal to the surface, thus the whole available surface is passivated. The SiO_2 uniform layer has the double function of reducing the losses from the defects in the surface of the photonic structure and in preventing the attachment of molecules and particles to the structures. Furthermore, it improves the coupling efficiency of the external source, i.e. lensed fiber, to the waveguide (side surface treatment).

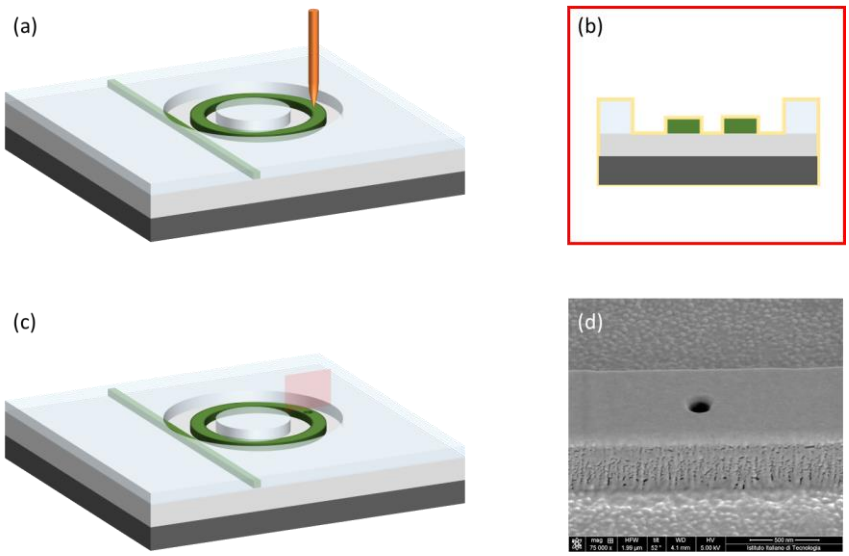

Figure 22 – (a) and (c) FIB milling of the hole passing through the whole ring resonator thickness. (b) A 2nm SiO2 layer (in yellow) is deposited by ALD to passivate the surface and prevent molecules adhesion. (d) SEM image of the perforated waveguide.

3.2 Optical setup

The purpose is to characterize the designed structure, in particular the hole acting as a point-like source. A custom-modified WITEC microscope [7] is used to perform both the optical characterization and fluorescence measurement described in the next chapter.

For the measurements performed for the optical characterization of the device and for its application for single particle detection, we used two different configurations: one in which the sample is placed vertically, and the radiation emitted by the bus waveguide coupled to the ring resonator is measured. In the second configuration the sample is placed horizontally and the radiation emitted by the hole is detected. I will indicate the two structures as "vertical configuration" and "horizontal configuration", respectively. In this chapter I focus on the description of the setup adopted for these specific measurements on the point-like source, i.e. the horizontal configuration.

A single mode lensed optical fiber (AMS Technologies – TSMJ-X-780/5) coupled to the laser source is placed on a 2-axis positioning stage, while the sample is fixed onto a 3-axis positioner. This allows the maxim degree of freedom needed for the alignment procedure. Positioning the sample on the 3-axis positioner allows to align in the xy-plane the hole acting as point-like source

with the detection system (that can be moved only in z-direction). The third direction is used to align the input port of the waveguide with the lensed fiber. The latter is brought in the correct lateral position by using the 2-axis positioning stage. A camera from top is used to monitor the alignment procedure and preliminary evaluation of the output from the hole. When the lensed fiber is brought close to the input port of the waveguide, the relative position is fine tuned to get the best coupling condition by monitoring the light scattered from the holes. Rough alignment for the starting position it is facilitated by the presence of specific guiding slits made during the manufacturing phase. A sketch of the setup and a photograph of the sample positioning are reported in Figure 23.

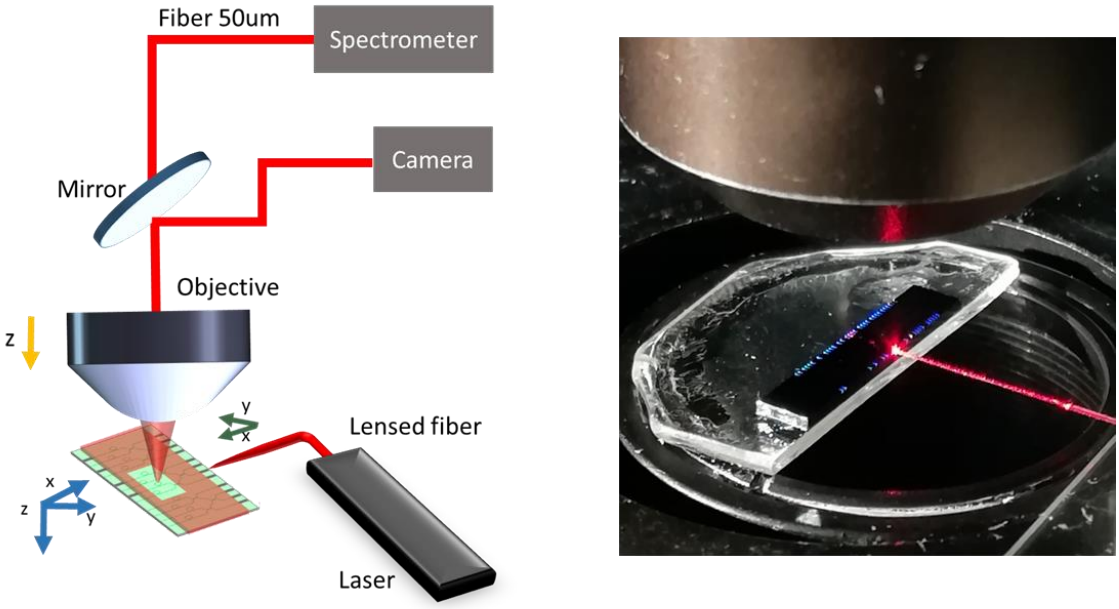

Figure 23 - Optical setup adopted for the optical characterization. Basic horizontal configuration. A laser source is used to excite the structure by means of a lensed fiber. The radiation emitted from the holes is collected by an objective from top. The sample positioning and fiber alignment is performed by monitoring the light emitted from the holes by mean of the camera. The collected radiation is thus sent to the spectrometer to align the position of lecture and to perform the measurement.

Supercontinuum source

The laser source coupled to the optical fiber to perform the optical characterization of the device is a supercontinuum white light laser (SuperK EXTREME) in the visible range (*400 nm - 850 nm*). The system consists of two parts, one part is the actual light source, the white light emitted is

brought into the second part of the system, which is a filtering system. An Acusto Optic Tunable Filter (AOTF) allows to select up to 8 wavelengths simultaneously. It is also possible to select the power of the emission *via* software.

Monochromator

Using a continuous source, the role of the monochromator becomes fundamental. Here, the monochromator integrated in the instrument (Witec UHTS 300) has been used. The spectrometer has a double grating: one grating with 600 lines/mm (resolution *0.09 nm*) and the other of *1800 lines/mm* (resolution *0.025 nm*) equipped with a CCD (charge coupled device) camera.

For the transmittance spectra, the *1800 lines/mm* grating was used.

The spectral range covered by the spectrometer as well as the spectral resolution depends on the employed CCD camera, the position of the turret and the grating. The camera provided in the used Witec custom-made setup is a CCD Camera DU970N-BV (EMCCD), with a 1600×200 array of 16μm square pixels with thermoelectric cooling down to -100°C (used at -58°C). By adopting the crop mode, thus reducing the spectral range investigated during the spectral acquisition, it is possible to accelerate the measurements up to 1500 spectra per second. This means being able to monitor the shift of the resonance peak with a temporal resolution of about *700 μs.*

3.3 Optical characterization of the device

3.3.1 Background free (SNR)

The high spatial confinement of the EM-field generated by the sub-wavelength hole is a point of strength offered by the studied structure. The high signal-to-background ratio is crucial for the different possible measures on chip. Here the background is intended as the contribution of the laser scattered inside the sensing chamber, indeed several contributions can be given by the EM-field scattered from the surface of the ring resonator (scattering losses), the scattering light coming from the region of coupling between the waveguide and the ring resonator and the contribution given by the scattered light from the coupling of the lensed fiber with the input port of the waveguide. We can indicate this contribution as background and thus speak about signal/background ratio. For example, as we will see later, the point-like source leads to the background-free measurement condition, increasing the sensitivity of the tests and reducing the

noise from the particles external to the source, thanks to the high spatial selectivity of excitation even in high dense. More attention to the dependence of losses on size is paid in the next paragraphs. Here we limit to verifying that the background is constant in the different measurements and coincides with the white noise of the acquisition system, thus proving that it behaves like a point-like source with an intrinsically low noise.

The measure is carried out analyzing the image plot profile related to the radiative losses at each hole (holes of different diameter) detected in far field by the high numerical aperture objective. The picture of the sample under white light illumination, in order to make the structure evident, and that of the sample under excitation by lensed fiber are reported in Figure 24, panel (a) and (b) respectively. The image plot profile was studied in order to evaluate the less favorable condition for the S/B ratio, in fact it was plotted along the ring profile, where the losses from the resonator can contribute to the background signal. The image line profile over the lines *I*, *II* and *III* corresponding to the holes of *80 nm, 100 nm* and *150 nm* respectively, are reported in panel (c), from top to the bottom. Over each plot is reported the zoomed image of the correspondent point-like source.

From the different intensity profiles we can see that the background is constant in the three positions and coincides with the white noise of the detection system, the radiation recorded at the different holes instead becomes larger as the size of the hole increases.

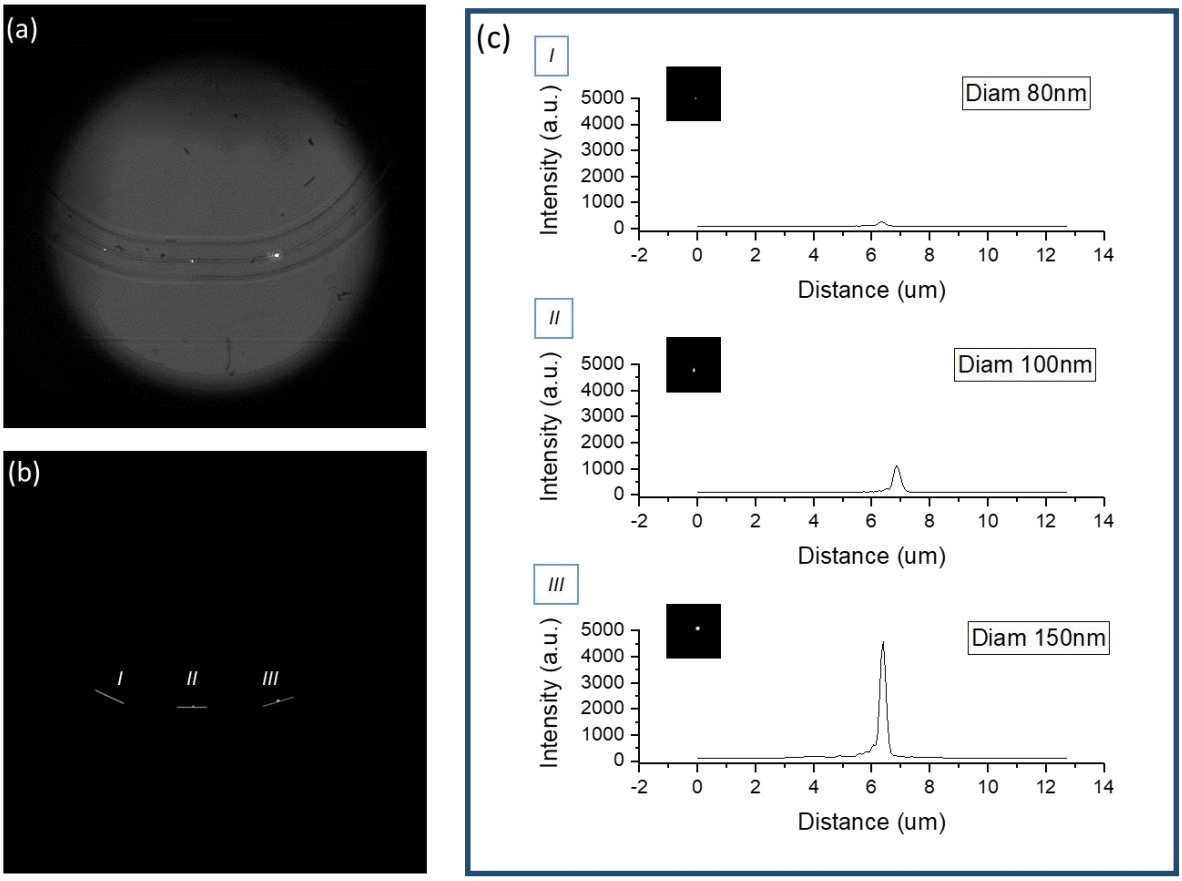

Figure 24 - Scattering light from holes with different diameter and relative image plot profile. (a) Picture of the sample under white light illumination from top and excited by the lensed fiber. (b) Sample excited by lensed fiber, the three holes act as point-like source and are visible from the scattered radiation. At each hole a line corresponding to the image line profile is superimposed. On panel (c) from top to the bottom the image line profile over the lines *I*, *II* and *III* are reported in order. The lines correspond to the holes of diameter 80 nm, 100nm and 150 nm respectively. In each box is also show the zoom of each point like area.

3.3.2 Radiative losses from the hole in ring resonator and waveguide)

In the previous chapter we presented the analytical model that allows to associate the variation of the ring resonance modes (splitting and damping) with the size of the scatterer present in the resonant cavity.

Similarly to the discussion carried out by Zhu et al.[6], we found the dependence of the above parameters on the size of the scattering element. In particular, for a through hole of radius R milled in the ring resonator, the splitting of the modes is given by

$$\delta = 2g = -\frac{\alpha f^2(r)\omega_c}{V_c} \tag{3.1}$$

and the radiative loss factor associated with the coupling of the mode to the scatterer is defined as

$$\Gamma_R = \frac{\alpha^2 f^2(r) {\omega_c}^4}{6\pi v^3 V_c} \tag{3.2}$$

The dependence on the radius of the cavity acting as defect is given by the polarizability, that within Rayleigh approximation, is

$$\alpha_y \sim \frac{4\pi a}{3} \frac{(\varepsilon_1 - \varepsilon_m)(4R^2 - a^2)}{(4R^2\varepsilon_1 - a^2\varepsilon_m)} \tag{3.3}$$

The emission (radiative losses) from holes of different sizes, with variable diameters in the range *60 nm- 200 nm*, was studied. Figure 25 shows the SEM pictograph of the perforated racetrack (a) and the fraction where the holes are milled at a mutual distance of $5\ \mu m$ (b), together with a picture of one of the different holes. A closer view of one of the perforated hole is shown in Figure 25.c.

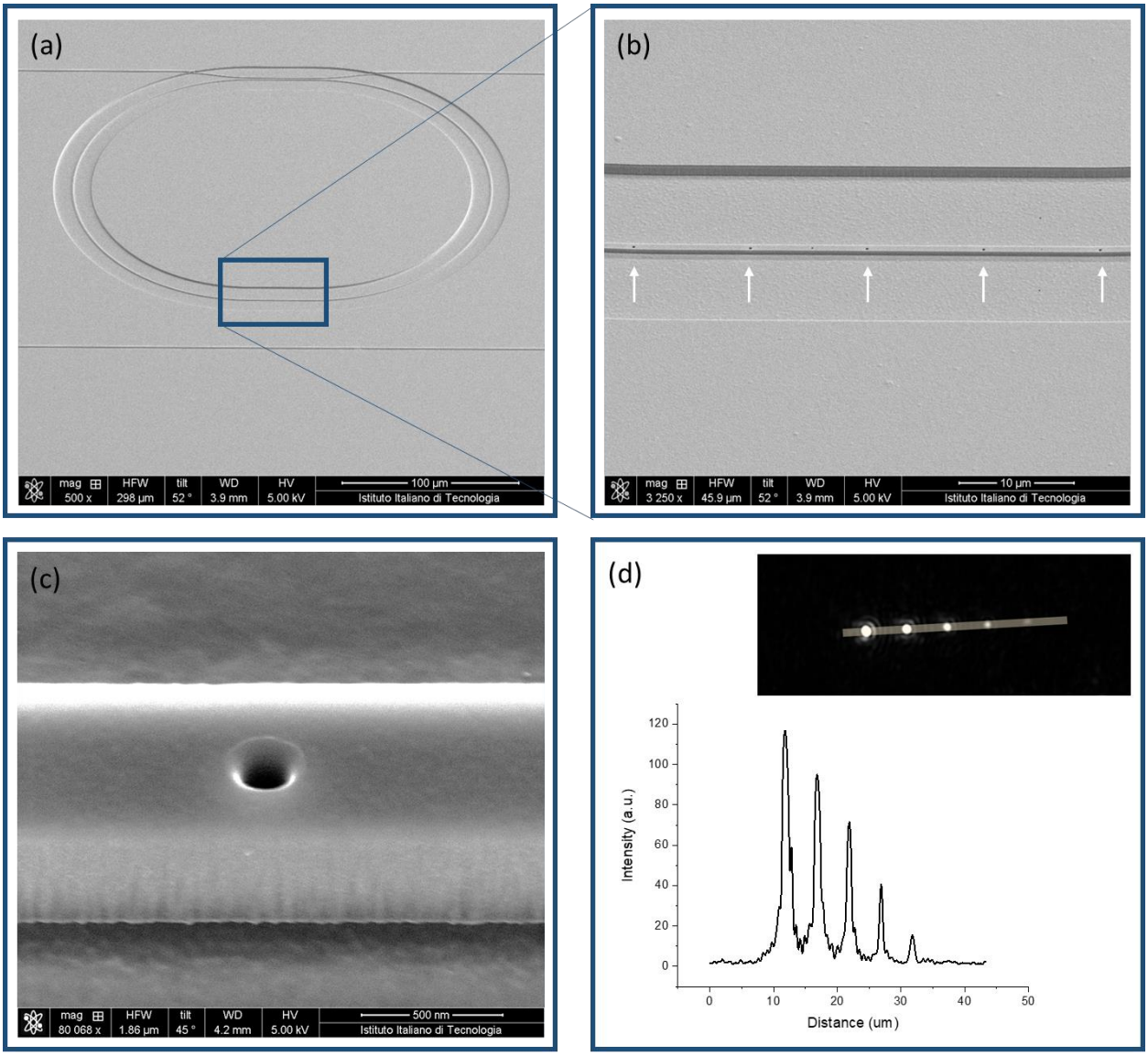

Figure 25 - Racetrack perforated with holes of variable diameter. (a) SEM pictograph of the racetrack analyzed. The blue box marks the area where the hole are milled. (b) SEM pictograph of the blue box superimposed on panel (a). The SEM pictograph shows the racetrack waveguide with the five holes with diameter respectively from left to right of 198 nm, 174 nm, 125 nm, 96 nm, 64 nm. The white arrows serves as guide for the eyes to see the holes. (c) SEM pictograph shows a close view of the hole with diameter 125 nm. (d) Image plot profile in correspondence of the perforated area of the racetrack. The inset reports the image recorded with the camera on top and used for the analysis. The contrast of the image is here opportunely enhanced to make all the holes visible. The yellow line indicate the profile analyzed.

The model illustrated shows the dependence of radiative losses as a function of the hole, considering the arrangement of modes in the volume and in the resonator, together with a series of specific parameters of the model. The experimental measurement allows to collect only a portion of the emitted radiation so we limit to verify the dependence of the measured observable (radiative

losses) on the size of the hole. The line profile obtained by opportunely tuning the line width so to include the whole emission from the holes, was analyzed measuring the area under the curve at each hole. The graph reported in Figure 26, reports the dependence of these value, ascribable to the radiative losses, as function of the radius of the hole. The data were fitted with a simplified function underlying the dependency on the radius of the hole, as per the definition of the radiative loss factor given in eq. 3.2. The fit shown, to be intended in a qualitative way, verify coherence of the data with the model.

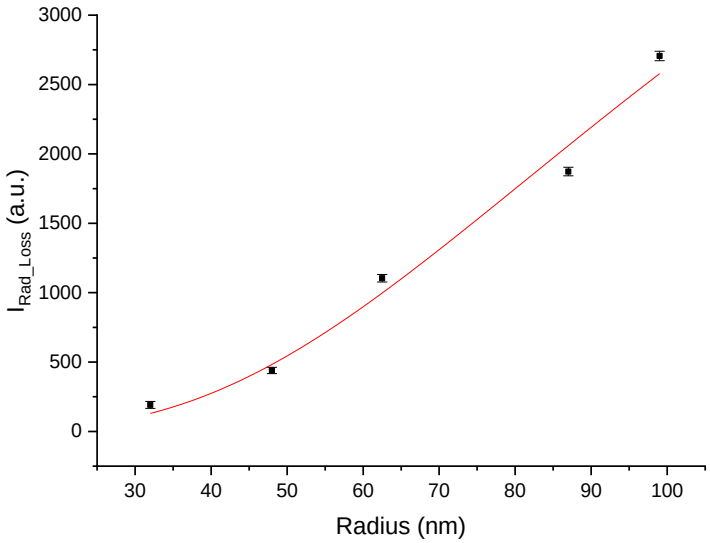

Figure 26 - Radiative losses dependence on the radius of the hole perforated in the ring resonator.

It has been said that the resonant cavity supports two degenerate propagating modes, with the same resonant frequency and field distributions but opposite propagation directions. Inserting a sub-wavelength hole disturbs the symmetry of the system, and the two modes will interact with each other in a constructive/destructive way. The resonant structure of the ring is fundamental in order to exploit the photonic waveguides as biosensors for several factors, one of the major is the possibility of working in multiplexing configuration. The same possibility must be preserved in the perforated ring system, in particular as regards the integration of the optical system with the immunofluorescence assays. The cornerstone is that the hole acts as a point-like source. By inserting several holes in a single ring, these too will behave as point-like sources. In order to obtain a more accurate measurement, it is important to be able to treat the sources practiced in the

same ring in the same way, i.e. the ideal case is to have sources in which the field is equally uniform and highly confined.

Experimentally, it is found that the loss factor associated with holes of equal diameter in the ring remains constant from one to the other.

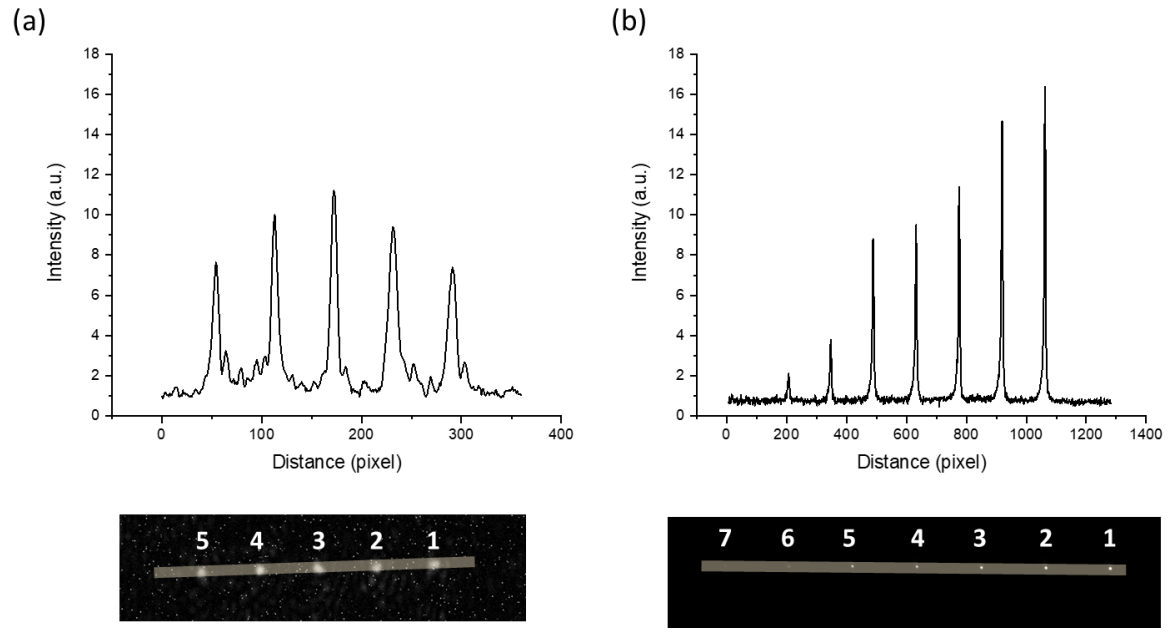

Figure 27 - Image of the scattering losses below and relative image line profile above for holes of the same diameter (100 nm) in racetrack (a) and waveguide (b).

It can be argued that the use of a resonant cavity is not essential in order to obtain a point-light source in a photonic integrated system. A sub-wavelength hole in a simple dielectric waveguide acts as a point-like source with a high signal-to-noise ratio, as per the case of the ring resonator.

Such a system is very convenient for approaching the optically confined and guided system, bypassing the loss factor due to the coupling efficiency of the waveguide-ring system. In fact, in the case of the ring resonator, the radiation that is not emitted by the hole continues to resonate in the ring and therefore continues to partly re-couple to the hole. This makes all the holes see a similar EM-field and therefore the losses from them will be similar. This is not the case with the straight waveguide, which is the case of a single pass structure. Thus, without the resonant factor, there is, among other things, a constant decrease in the coupled light in successive holes. This different behavior limits the use of straight waveguides in sensor platforms. A possible compromise between the two structures is to use waveguides with semi-reflective walls, so as to

induce a resonant cavity in the waveguide. This would allow to avoid the limits of EM-field intensity inside the resonator due to the coupling efficiency and losses between bus waveguide and ring resonator. Figure 27.b reports the case of a single waveguide, in which holes of constant size ($100\ nm$) and distance ($5\mu m$) comparable to those made in the ring resonator have been made. The comparison between the two panels in Figure 27 cannot be made in terms of overall intensity since the integration time characteristic of the acquisition of the two images differs, due to the different excitation conditions and efficiency. The aim is to compare the distribution of the losses, or rather the trend of the losses in the holes within the different structures.

It is noteworthy that the hole in the ring resonator is a low-noise point-source, and allows for a double detection configuration. The EM-field confined within the hole is a strong near field source. When a molecule/particle is close to or enter inside the hole, the near field excite the molecule that will re-emit in an isotropic way at a distinct frequency. A part of the emitted radiation will resonant component will couple back to the ring, where only the resonating component will interact constructively and follow the same path of the incoming radiation coupling to the bus waveguide, allowing in this way to read the radiation emitted directly from the output port of the bus (vertical configuration, chapter 4, Figure 31). The remaining part of the emitted radiation is emitted in the far field, allowing an out-of-plane detection (horizontal configuration, chapter 3, Figure 23).

3.3.3 The propagating modes inside the resonant structure

WGM resonators are generally studied by means of tunable lasers, the range of the spectrum of interest is investigated by tuning the frequency of the laser source. By tuning the coupled wavelength the transmittance spectrum could be recorded and the modes of the cavity are read in the transmittance spectra. The best condition for this measurement is fulfilled when for resonance wavelength, no light is coupled back from the resonator to the waveguide, thus no signal is emitted out from the waveguide at the resonant wavelength.

Our aim is to exploit the through hole as a point-like source. The optical configuration is slightly different from the one just described (paragraph 3.2, Figure 23). Indeed a supercontinuum laser (NKT SuperK extreme EW12) is used as a broad band “white” laser source. The characteristic emission spectra are collected, directly from the hole, by the upper objective and read by the Witec monochromator (see page 54 for details).

The whole available wavelength range (400 – 850 nm) is investigated and resonating modes were collected as function of the external media (air and water).

Resonance modes are extremely sensitive to the refractive index variation of the external solution, this is the basis of the operating principle of the sensor in the "bulk sensitive analysis" configuration. Technique in which the variation of the refractive index of the whole solution is sensed by monitoring the shift of the resonant modes. Moreover, it can be seen that the variation of the sensed solution implies a modification in the optical performances of the resonant structure. In fact, a lower contrast of the refractive index of the guide compared to the external one determines a lower confinement of the WGM into the resonant structure. This affects the scattering losses and radiative loss factors and therefore the overall Q-factor.

Figure 28 shows the characteristic spectrum emitted by the ring with air or water as an external medium. Is remarkable that the resonance peaks have a lower FWHM in the case of waveguide embedded in water, i.e. the quality factor of the resonator is higher.

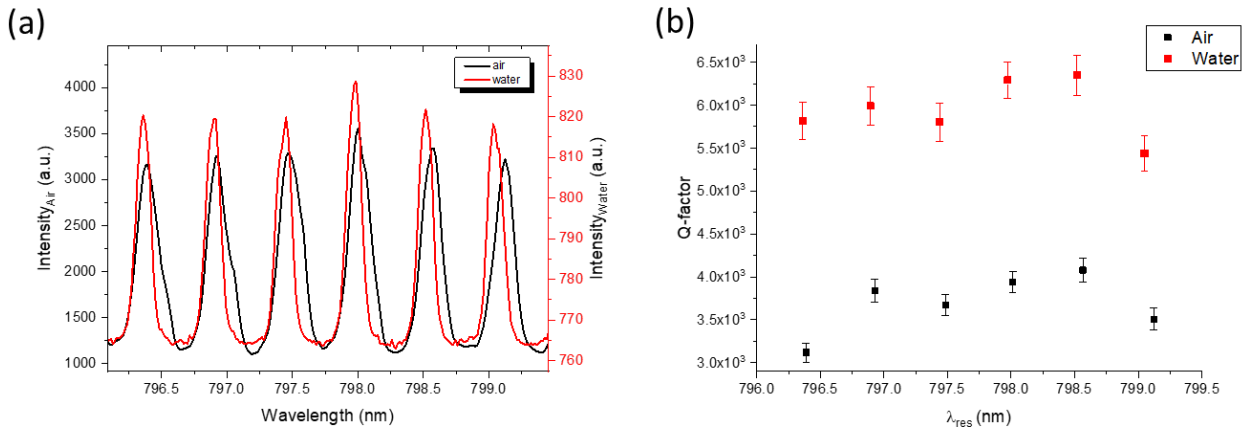

Figure 28 – Resonant modes propagating inside the racetrack. (a) Characteristic emission spectrum acquired from the hole made into the racetrack in air (black line) or in water (red line). (b) Quality factor of the resonant modes for the two environment: air (black line) and water (red line).

Is worth to being highlighted that at longer wavelengths, the splitting of the degenerate resonance mode can be distinguished. Comparing the emission of the same resonant mode in the two systems (air and water) we see that the splitting is solvable in the case of air while for water the distinction remains unresolved even if the mode is narrower overall (higher Q-factor). In fact, the refractive index of water (n = 1.33) is more similar to that of silicon oxynitride (n = 1.66) in respect to that

of the air (n = 1), thus the induced splitting is greater. It is worth to note that at higher wavelengths it is possible to resolve the splitting under both conditions. The quality factor of the resonant split mode is estimated. Both the values are reported in Figure 29, where the inset reports the analyzed modes.

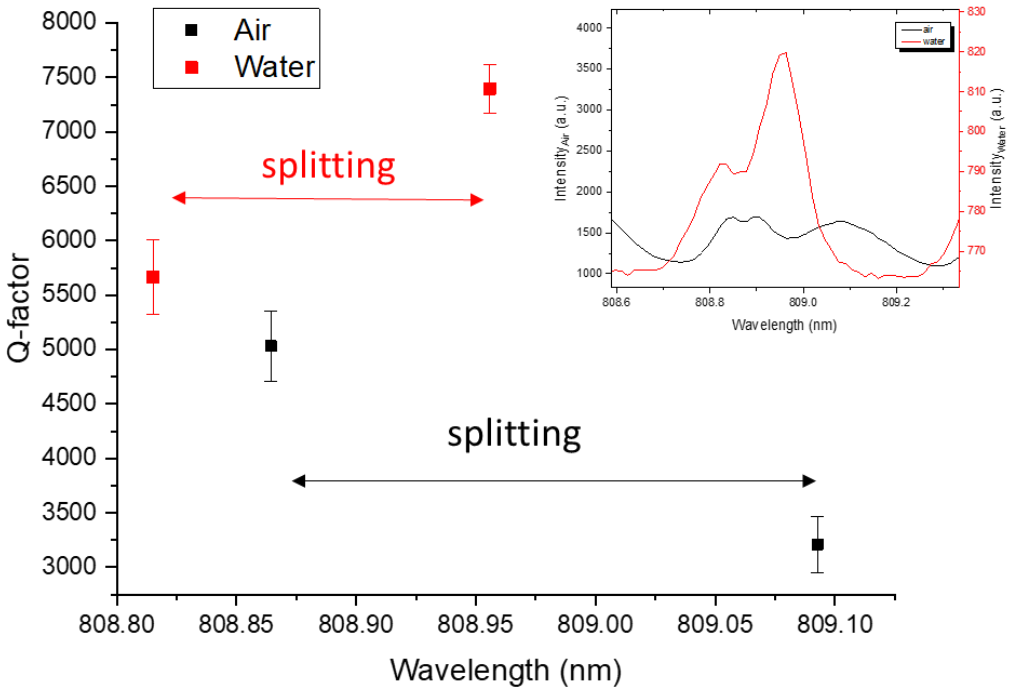

Figure 29 - WGM splitting in air (black) and water (red). The inset reports a close view of the resonance mode analyzed in case of the different media: air (black) and water (red).

3.4 Architecture for label free single particle detection

For a label free (labeless) particle detection with ring resonator the key role is played by the modes shift. When a single nano-object binds on the surface of the resonator the resonance of the structure shift (or broadening, or splitting). By looking at the temporal evolution of the binding curve, it is also possible to extract information on the molecular dynamics on the surface of the resonator.

Generally, in surface sensitive techniques, the surface of the ring resonator (coinciding with the active area) is decorated with biomolecules acting as binding sites for the analytes that aim to be

detected. Considering a system without any kind of functionalization with bind sites for the molecules is still theoretically possible to detect the presence of a particle and to monitor its diffusion by observing the split resonance modes of the WGM resonator, which can be distinguished as an active mode and an inactive mode.

For convenience and clarity we report in Figure 30 the image described in paragraph 2.4.1 (Figure 14) of the cross-section of the ring showing the distribution of the two modes with respect to the hole (Figure 30, panels (b)-(e)), and the change in the transmittance spectrum induced by their interaction with a particle (Figure 30(a)).

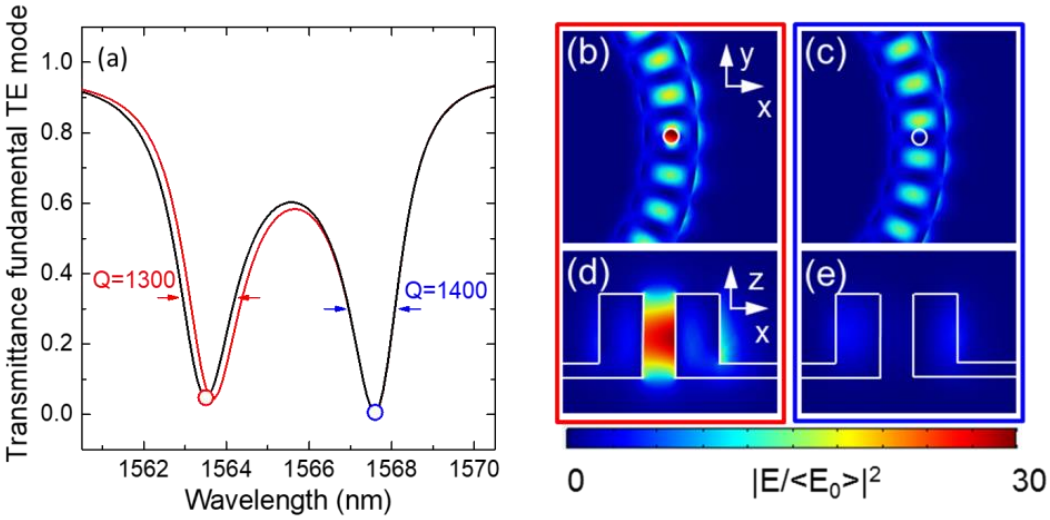

Figure 30 - (a) Characteristic modes distribution guided within the perforated ring resonator, fundamental TE mode. Reference spectrum (black curve) of the unperturbed structure superimposed on active (red) and inactive (blue) modes that sense the presence of a particle inside the hole. Titania bead of 80 nm diameter and refractive index n=2.4. Refer to Figure 14 at paragraph 2.4.1.

As we can see clearly from the Figure 30, the inactive mode is kept shielded from the particle thus remains un-shifted. On the contrary, the active mode resonance undergoes a redshift. Single particle detection for unlabeled media could be carried out by monitoring the shift of the active mode peak during the interaction particle-structure. The peak variation of the inactive mode is determined by the noise related to fluctuation of the laser intensity and frequency, thermal noise, noise detector and environmental disturbance. By using this peak (inactive) as a normalizing factor for the shift of the second peak (active), the external contribution to the noise of the measurement could be monitored and suppressed.

One of the main constraints that limit the use of this technique are related to the time of diffusion of the particles within the extremely confined sensing volume. The limiting factors depend on the configuration chosen. Using the tunable laser as light source, limits are the scanning time of the wavelength in the range related to the mode being analyzed and the sampling rate of the detector. On the other hand, using a supercontinuum laser, the speed is limited by the time of acquisition of the spectra through the monochromator.

Here we design a possible approach to the implementation of this method for single particle detection in a non-functionalized (label free) platform.

From the results of the simulations (figure 19), the shift of the active mode offers a small margin for the application of this technique considering the spectral resolution of the instrument (*0.025 nm*). On the other side, the possibility of working within the crop mode of the camera allows to reach a temporal resolution of about *700 μs*, as previously described in paragraph 3.2. The application of this approach for perform on chip single particle detection in full-label-free configuration can be an interesting further perspective for the use of the device.

[1] M. G. Wood, L. Chen, J. R. Burr, and R. M. Reano, “Optimization of electron beam patterned hydrogen silsesquioxane mask edge roughness for low-loss silicon waveguides,” *J. Nanophotonics*, vol. 8, no. 1, p. 083098, 2014.

[2] H. Namatsu, “Three-dimensional siloxane resist for the formation of nanopatterns with minimum linewidth fluctuations,” *J. Vac. Sci. Technol. B Microelectron. Nanom. Struct.*, vol. 16, no. 1, p. 69, 1998.

[3] A. E. Grigorescu and C. W. Hagen, “Resists for sub-20-nm electron beam lithography with a focus on HSQ: State of the art,” *Nanotechnology*, vol. 20, no. 29, 2009.

[4] C. Reyes-Betanzo, S. A. Moshkalyov, M. A. Pavanello, A. C. S. Ramos, and J. W. Centro, “Plasma etching of Si3N4 with High Selectivity Over Si and SiO2,” *Proc. SBMicro2001-XVI Int. Conf. Microelectron. Packag.*, vol. 2, pp. 70–75, 2001.

[5] Y. Chen, J. Feng, Z. Zhou, C. J. Summers, D. S. Citrin, and J. Yu, “Simple technique to fabricate microscale and nanoscale silicon waveguide devices,” *Front. Optoelectron. China*, vol. 2, no. 3, pp. 308–311, 2009.

[6] J. Zhu *et al.*, “On-chip single nanoparticle detection and sizing by mode splitting in an ultrahigh-Q microresonator,” *Nat. Photonics*, vol. 4, no. 1, pp. 46–49, 2010.

Chapter 4
Single particle detection

This chapter is dedicated to the use of the ring structure to perform single molecule detection using fluorescence. Indeed, fluorescence-based assays are the extremely common and often assumed as gold standard for single molecule detection. A very large number of single molecule sensors exploits the single molecule fluorescence [1], however the technologies developed and currently in use presents some limits.

The first part of this chapter briefly introduce the issue of fluorescence-based assay, illustrating what are the major challenges and technologies used to address them. Secondly, the method and the results obtained are reported and discussed.

4.1 Fluorescence-based assays

Among the several optical methods that have been developed for biological and chemical investigations, fluorescence microscopy is the most common, particularly in the field of detection or analysis of individual molecules. In fact, fluorescence is a very powerful technique for its high optical efficiency and for the information it is able to provide. For example, parameters such as lifetime, brightness or spectrum are sensitive to the molecular structure and the molecular environment. The techniques developed to perform analysis of single particle work under conditions of low concentration, i.e. limited number of particles within the excitation volume. A clear example is the case of fluorescence correlation spectroscopy (FCS), a very important technique which will be discussed later. This is a statistical technique that, under standard conditions, allows the measurements of the diffusion of a single particle to be carried out in solutions at nanomolar concentration. So as to have a few molecules in the volume of measurement that is in the femtoliter range, state of the art is $0.2\mu m^3$ ($0.2\ fL$). Nevertheless, this condition doesn't match the biological one. Indeed, molecular concentrations in the cell membranes or more generally in living cells are generally quite large, commonly in the range of micro to millimolar.

Many enzymatic reactions occur naturally under conditions of ligand concentration of the order of micro to millimoles and reducing this concentration can change their functionality and thus affect the measure.

This shows the need to considerably reduce the volume of analysis, arriving at nanometric dimensions. An extraordinarily small excitation volume allows the condition of a few particles/molecules in the volume itself, even in biologically relevant media.

Different methods and techniques have been developed for this purpose. Total Internal Reflection (TIRF), for example, uses as active field to perform sensing experiment the evanescent field that is obtained by making the laser excitation beam impinge on the surface of the sensor with an angle higher than the critical angle (Snell's law). Taking advantage of this exponentially decaying field, thus playing on the depth component of the field, it is possible to significantly reduce the detection volume. The limitation is given by the absence of lateral confinement of the same. In any case the field is reduced by about a factor of ten [2]. Another approach is to work in super-resolution regime, as in the case of stimulated emission depletion (STED) microscopy [3]. This reduces the total volume by about 5 times.

Alternative methods are those involving the reduction of the detection volume mechanically. This can be done by using nano- or micro-channels appropriately designed or with near field scanning optical microscopy (NSOM). These techniques led to observation volumes of up to tens of attoliters [4] or zeptoliters [5], respectively. The latter approach allows for an incredible reduction in volume, but is limited by the complexity of probe fabrication and the difficult implementation in parallel processes.

A third approach is the use of nanometric openings in continuous opaque metallic films. Among the different possibilities mentioned, this technique is undoubtedly the most widespread and promising in the application as on chip single molecule/particle detection and deserves special attention as we can assume it as a state of the art and reference point for our device [6], [7].

The case of a single nano-aperture in an infinite and perfectly conducting metallic film was first modelled by Bethe [17] and Bouwkamp [18]. This model describes the evanescent field produced by a sub wavelength aperture, for a linearly polarized plane wave, showing that the transmission of the radiation scales with the ratio of r to the wavelength at the power of four according to the simplified expression

$$\eta_B = \frac{64(kr)^4}{27\pi^2}$$

Where r is the radius of the aperture and $k = 2\pi/\lambda$ indicates the norm of the wavevector of the incoming light [19]. The above equation refers to the approximation of a circular aperture of radius *r* equal to the side of the square aperture for which exact solution is given in [17].

In the real case however, the layer has a finite thickness and the nanometric apertures show waveguiding properties. The confined lateral dimension of this waveguide modify the dispersion relation of the electromagnetic field, determining a specific wavelength λ_c for which the light cannot propagate through the aperture, this wavelength is therefore indicated as cut-off wavelength.

When the aperture diameter is sufficiently small beneath the cutting diameter of the fundamental excitation mode, the light within the aperture is limited to a fast-decaying evanescent mode, with a decay length of tens of nanometers. Since light is not allowed to pass through this tiny aperture, these devices are referred to as zero mode waveguides (ZMWs). It follows that for some incoming light, the electromagnetic field remains confined to the bottom of the nanoholes, and only the very small portion of molecules located in this region can be detected. The rest of the molecules are shielded from the metal film, so it does not feel any light excitation.

ZWMs allow to obtain detection volumes up to 6 orders of magnitude lower than that of the standard confocal microscope, reaching volumes in the order of the zeptoliter [8]. The zero mode waveguides are widely used in the field of DNA sequencing [9] or in the study of DNA-protein interaction [10], [11]. Finally fluorescence enhancement in ZMWs has been demonstrated theoretically and experimentally [12], [13].

The possibility of having point sources integrated in the photonic waveguides offers several advantages. In particular, it allows for an extremely confined field source on chip, thus maintaining the advantages of the potential miniaturization and integration of multiple sensing structures on a single platform. Furthermore, being a fully dielectric structure, no fluorescence quenching due to the metal proximity affects the measurement.

In the studied structure, the detection volume is determined by the arrangement of the resonant mode inside the through hole made in the ring resonator and is in the order of the zeptoliter, as in

the case of the ZMWs. Moreover, as per the simulations carried out, it is seen that the hole produces an enhancement of the local field, thus increasing the sensitivity of the fluorescence measurement.

4.2 Design of the experiment

4.2.1 Setup

The setup used for the experiments is sketched in Figure 31.a. A single mode lensed optical fiber is coupled to the HeNe *632.8 nm* laser and is fixed on a 3-axis positioner. The sample is fixed to a 2-axis positioning stage and transmitted radiation is collected at the outport of the waveguide by an objective. In particular, 20X Zeiss, N.A. 0.4.

The collected light is filtered by a dichroic beamsplitter filter for *633 nm* and read with a detector. Two additional filters are placed in the optical path, selected in order to reduce noise and maximize reading efficiency. The portion of the beam deviated by the dichroic beamsplitter filter is collected with a multimode fiber and sent to a second detector. This signal is used as reference regarding the overall coupling of the system and monitoring the laser power coupled with the waveguide.

The oscilloscope (Lecroy wavesurfer 422) allows one to monitor and record the two traces simultaneously.

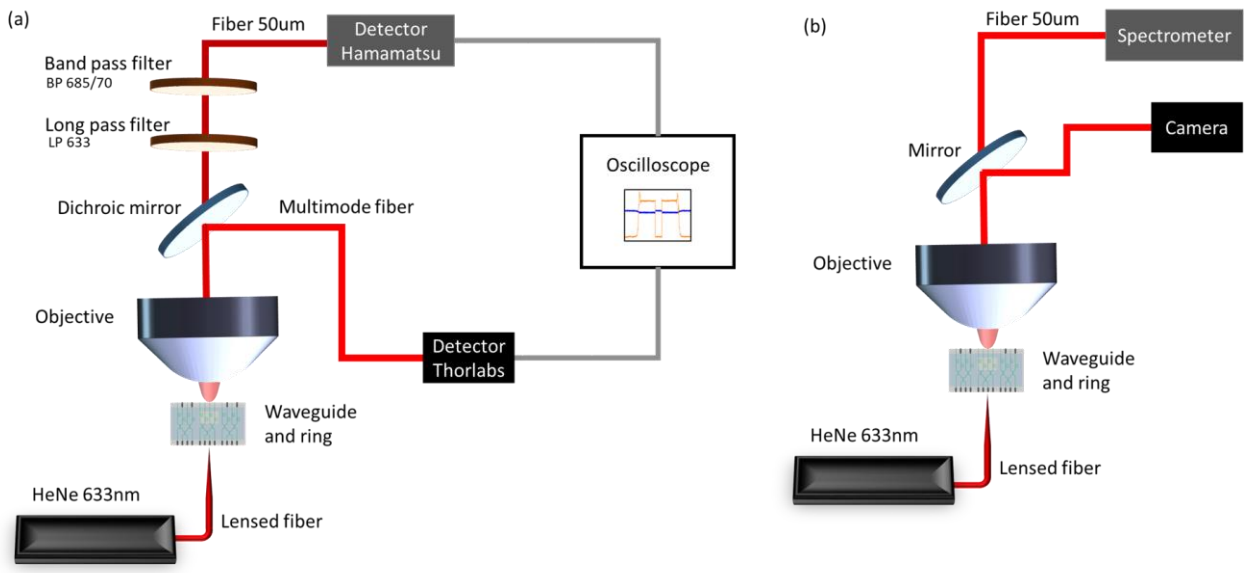

Figure 31 - Configuration used to perform fluorescence single particle detection (a). Configuration adopted for alignment procedure (b). Both can be described as vertical configurations.

Filters and detectors

The aim is to measure the fluorescence emitted by particles in the excitation volume, i.e. in the hole, as a component of radiation coming out of the guide. The fluorescence intensity is significantly lower than the excitation intensity, hence in order to reduce the noise of the measure as much as possible, the right combination of filters is crucial. The final configuration is chosen as the most efficient in filtering the laser and with the maximum overlap between the filter transmission bandwidth and the fluorescence emission spectrum of the probe.

Different filters have been tested: BP 680/42, BP 698/70, LP 633, BP 685/70. The combination that resulted best fitting our system involves the use of the Long Pass 633 (633 nm Semrock RazorEdge® ultrasteep long-pass edge filter) and the Band Pass 685/70 (Semrock 685/70 ET Bandpass). QDs are chosen as fluorescent probes due to their intrinsic high fluorescence efficiency (quantum yield).

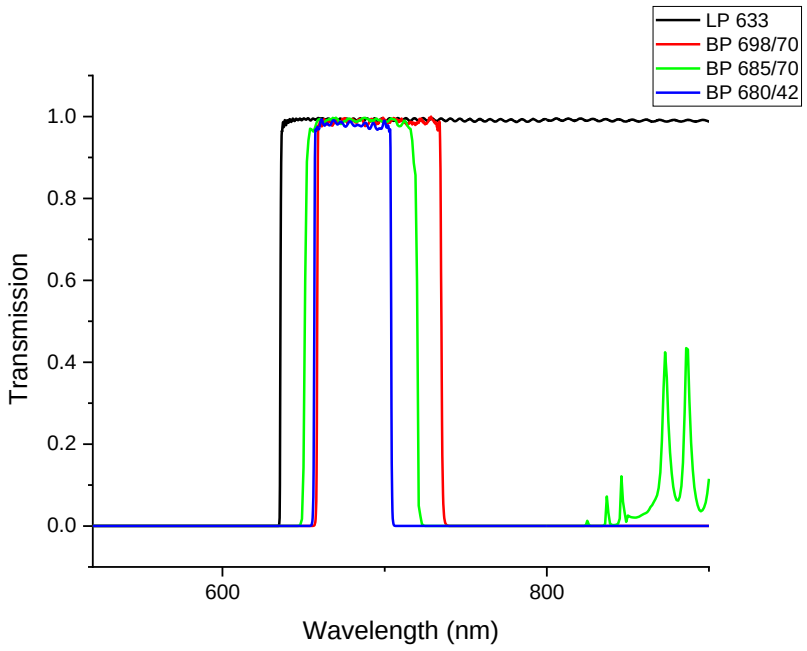

Figure 32 - Transmission of the different filters compared. 633 nm RazorEdge® ultrasteep long-pass edge filter (black), 698/70 nm BrightLine® single-band bandpass filter (red), 685/70 ET Bandpass (green), 680/42 nm BrightLine® single-band bandpass filter (blu)

Regarding the read-out system, the laser signal deviated by the dichroic mirror is read by an amplified detector with a wide wavelength range, Thorlabs (DET 100). The amplification factor has been set in order to match the non-saturating regime.

Fluorescence signal is recorded by a photosensor module (Hamamatsu H7422-20) that offers an high sensitivity over a wide spectral range, from *300 nm* to *890 nm*, and is integrated with a thermoelectric cooler that maintains the photomultiplier tube at low temperature to reduce the thermal noise. This allows one to obtain very high SNR even at extremely low light levels.

4.3 Single particle detection

4.3.1 Wettability and alignment procedure

Plasma oxygen treatment is performed to increase the wettability of the surface, then a PDMS gasket is aligned on the substrate to define the chamber for the particles solution. Finally, placing the sample in the vacuum chamber for a few minutes ensures that any air bubbles eventually trapped in the hole will be released.

Alignment plays a key role in this type of measurement. The coupling between the lensed fiber and the waveguide bus determine the efficiency of the system both in terms of the amount of light entering the guide and the excitation efficiency of the ring. On the other hand, the correct alignment of the reading apparatus to the output port is also crucial in order to collect the higher optical signal coming from the detection volume

The excitation fiber is brought in proximity to the waveguide input port using the 3-axis stage translators. The coupling condition is monitored with the upper camera/ monocromator by looking at the emission in transmission through the waveguide. In this phase, the signal is also detected by the spectrometer, as in the configuration (b) of the system (Figure 31.b). A finer alignment is performed by map scan. In particular, the system allows to scanning the substrate in xy-plane and collecting the spectrum point by point. Integrating only the signal at *633 nm* is possible to reconstruct a map of the emitted light. Then the sample is positioned centering the point showing the maximum intensity. This can slightly move the fiber-guide reciprocal position, so the maximum coupling is obtained by moving again the 3-axis stage translators and iterating the overall alignment process. It is worth to note that also z-position of the detection is corrected by acquiring map scan at different z of the objective. Figure 33 reports the procedure followed.

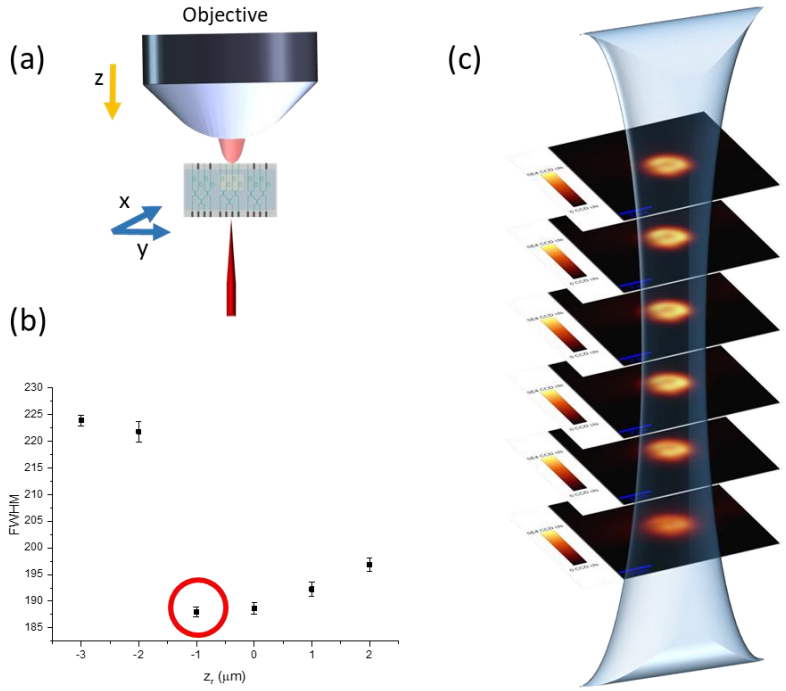

Figure 33 – Alignment procedure. (a) Sample is moved in the xy-plane to map the emitted signal point by point (blue arrows) and maps are acquired at different z-positions by moving the vertical objective (yellow arrow). (b)

FWHM as a function of vertical distance from the outport. (c) Schematic idea of the 3D map reconstruction from the emitted light at different z positions..

4.3.2 Fluorescence detection

In order to set the best condition for the excitation, the laser power was varied gradually from 0 to 1.2 mW. By simultaneously monitoring laser power and fluorescence signals coming out from the guide, it is possible to check whether the saturation condition of the probe (QDs) is reached. Moreover, a first measurement in water allows to verify the filtering of the laser radiation and to quantify the possible contribution to the intensity measured for the solutions with QDs.

An example graph is shown in Figure 34. Gradually increasing the intensity of the laser (black line) increases the emission of fluorescence (red line). Under saturation conditions, i.e. excessive excitation intensity compared to the maximum capacity of the probes (QDs) to absorb the radiation and re-emit it as fluorescence, a continuous increase of the laser signal is expected while the fluorescence signal remains constant. By monitoring this condition in real time, it is possible to verify that all measurements were made in linear regime.

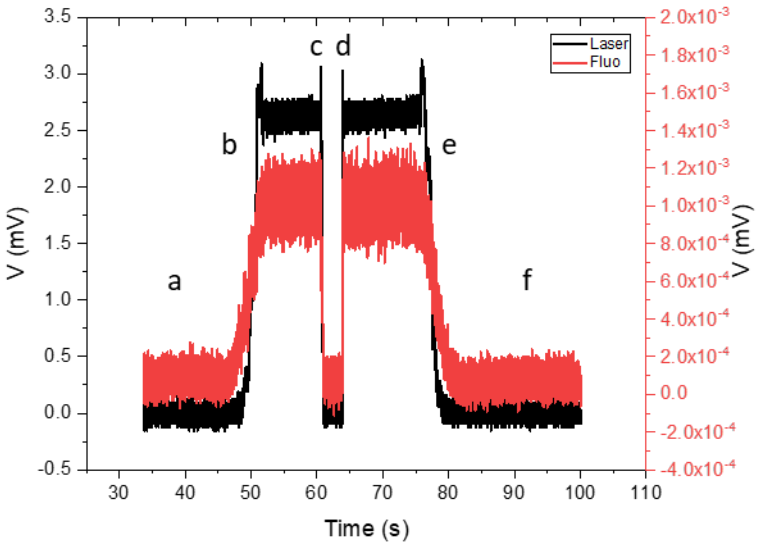

Figure 34 –Signal collected at the outport of the waveguide for a solution with QDs at a concentration of 10 ug/mL. Intensity of the laser (black line) and intensity of fluorescence (red line). Laser initially blocked (a) is gradually increased by opening the shutter (b). Laser is then shuttered quickly (c). Process run on the other way symmetrically. Quick opening of the shutter (d), gradual closure (e), stopped (f).

Aqueous dispersions of QDs at different concentrations have been investigated. We chose the concentrations according to the average amount of QDs in the volume of excitation (and detection), considering as an ideal condition that of one particle in a volume of the order of the attolitre. We tested the system also investigating cases in which statistically, in conditions of classical diffusion, not always there was at least one particle in the observation volume. In fact, as discussed below, the enhanced local field in an extremely confined volume can result in a modification of the diffusive motion of the particle, leading to a variation of the local density.

The sensitivity measurement of the system was carried out for both the ring resonator and the waveguide. In particular, in the case of straight waveguides, the case of a single hole (diameter *120 nm*) was studied. In the case of ring resonator, the first tests were made on racetrack with 5 holes of variable size (from *60* up to *200 nm*).

In both cases, a linear growth of the fluorescence signal is measured as the concentration increases. I summarize the results obtained by the racetrack in the Figure 35. The table on the side of the graph reports the concentrations and the estimated average number of QDs in the volume of detection. The number of particles statistically present in the excitation volume is estimated directly from the concentration of the solution.

In the case of the racetrack, the different holes with single volume in the range from $1\ aL$ to $10.8\ aL$, give an effective volume of $27.1\ aL$.

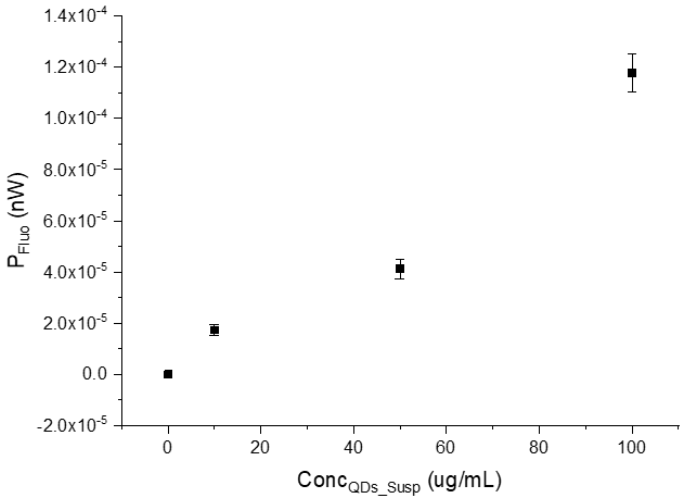

Concentration [ug/ml]	# QDs
Water	0
10	1
50	7
100	14

Figure 35 – Fluorescence recorded from the waveguide coupled with the perforated racetrack. Values measured at increasing concentration of QDs inside 5 different holes acting as point-like sources. The table reports the amount of particles estimated in the global effective volume for each solution.

A different effective volume is the one investigated in the case of straight waveguide, in which the active hot-spot is a single hole of 120 nm diameter, corresponding to a volume of 4.5 al. (Figure 36).

Finally, fluorescence-based single particle detection on chip was demonstrated both in case of waveguide and resonating structure.

The reasons that lead to consider the use of resonant structures instead of linear waveguides, lie in the perspective of application as on chip biosensor. In fact, the possibility of working in multiplexing is very important in this context. This is certainly a prerogative of the configuration with ring resonator, while it is less appealing in the case of straight waveguide. Exception is given by the possibility of creating a resonant cavity within the waveguide by depositing a reflecting and semi-reflecting layers at the extremities. This could be an interesting alternative and compromise between the ring resonator and the simple waveguide structures. The possibility of working with different sources in parallel has already been discussed in the previous chapter (paragraph 3.3.2). Further support for the use of resonant structures is given by the possibility of using the platform in flow-through configuration. Using the hole through the structure as a nanofluidic channel, it follows that this possibility offers further advantages in terms of detection efficiency. In this configuration, in fact, the solution is made flush through the hole made in the ring. Considering the nanometric diameter of the hot spot, which here also acts as a nanofluidic channel, it is thus

fundamental necessary to have more than one hole to have a total flow fast enough. Having more than one point-like source also allows you to solve the possibility that one of the holes occludes during the test. This last configuration offers several advantages for example the probability of interaction between the point-like source and the analyte and the velocity of the assay.

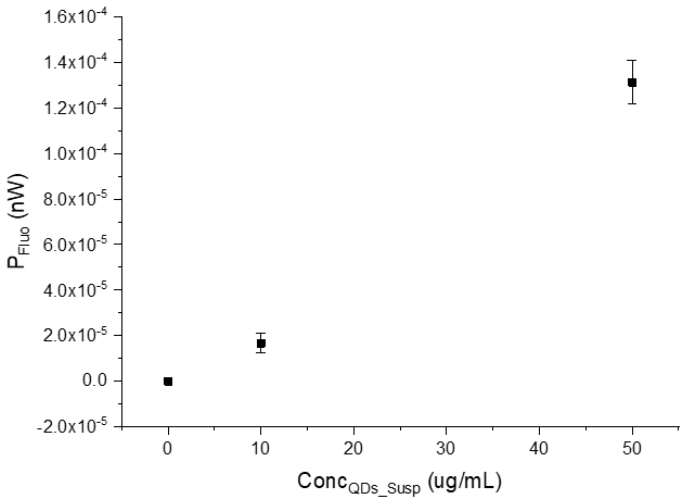

Concentration [ug/ml]	# QDs
Water	0
10	0.2
50	1

Figure 36 - Fluorescence in straight waveguide. Values measured at increasing concentration of QDs, single point-like source. . The table reports the amount of particles estimated in the volume of the hole for each solution.

4.4 Particles' diffusion

The result shown in the previous paragraph leaves open the possibility that the particle undergoes a deceleration or trapping effect within the excitation volume. I therefore considered the different techniques that could give me indications about the diffusive motion of particles in the volume.

The main technique for analyzing the diffusion of fluorescent particles in solution is Fluorescence Correlation Spectroscopy (FCS). This is a statistical technique which, by acting on fluorescence fluctuations, provides information about the number of particles within the excitation/detection volume and the type of motion to which they are subjected (random walk, drift, etc.). It is

applicable in diluted samples, where the detection volume contains on average a very small number of particles [14]–[16].

Although the analytical treatment necessary to model some configurations complicates the correct interpretation of the results obtained, the principle behind this technique is quite intuitive. When the fluorophore in solution passes through the detection volume, it is affected by the field and emits a burst of photons due to multiple excitation-emission cycles from the same fluorophore. The number of recorded photons depends on the velocity of the fluorophore passing through the excitation volume. The higher the rate of diffusion of the fluorophore, the shorter the time interval of the recorded fluorescence emission. Secondary factors can influence the measurement, for example photobleaching, generally avoidable under low power conditions. From correlation analysis of time-dependent emission, it is so possible to determine the amount and diffusion coefficient of the fluorophore.

The theory of FCS is based on Poisson statistics. Given a solution with on average N molecules in the volume of excitation, the probability that n fluorophores are present in the volume itself is given by

$$P(n, N) = \frac{N^n}{n!} e^{-N} \tag{4.1}$$

The variation in the number of particles in the volume determines a variation in the intensity of fluorescence. The faster the molecules move, the faster the intensity changes. The correlation of the intensity signal at time t and time $t + \tau$ therefore provides information about the diffusion of the particles and any forces that change their motion.

FCS measurements thus allow further characterization of the point-like source created in the ring resonator. This technique allows to obtain information on the dynamics of the particles inside the hole, and therefore on the effect of the field confined in the hole on the particles.

4.4.1 Experiment

We decided to analyze the diffusion of the molecules within the excitation volume taking advantage of the confinement induced by the hole. The measurement was then made in the configuration shown in Figure 37. As in the configuration adopted for the optical characterization of the point like source (paragraph 3.2), the excitation is carried out by a lensed monomode fiber coupled to the input port of the SiON waveguide. Fluorescence signal is collected by a water

immersion 60X objective (Olympus LUMPLFLN-W60X) at high numerical aperture (N.A. 1) and detected by a single photon counting module (xcelitas SPCM-AQRH-24-FC) combined with a timetagger unit (Swabian TimeTagger). Matlab script acquire and elaborate the signal according to the FCS technique [15], [16]. This configuration allows one to do measurements with a time resolution of up to *100 ns*.

The same laser source (HeNe 633nm laser) used for the optical characterization of the point-like source is used for this measurement. The ATTO633-NHS molecule is used as the fluorescent probe. This molecule has been chosen among the available probes because its excitation and emission curves best match the excitation laser and the emission filter set, respectively.

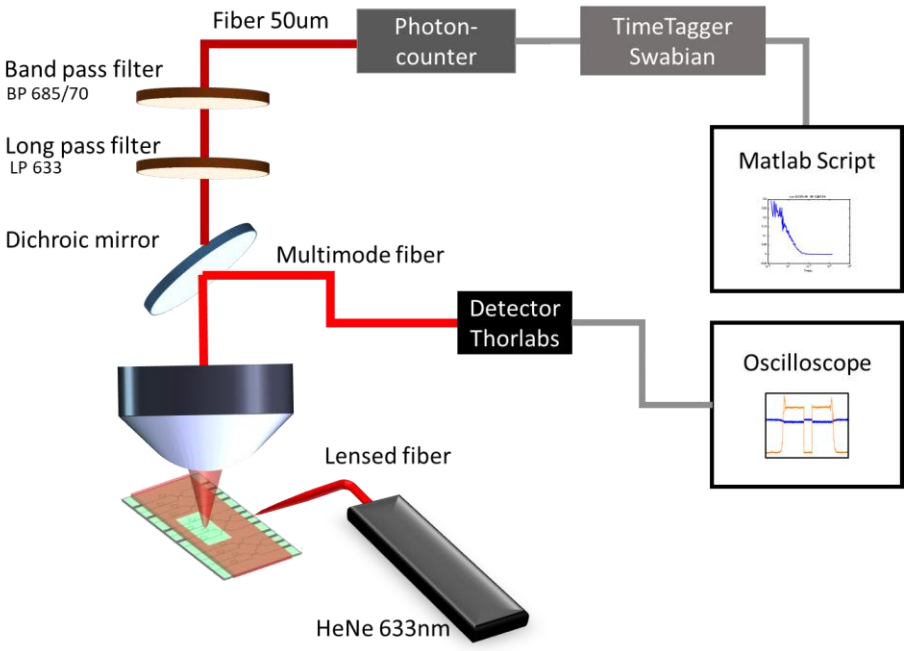

Figure 37 - Optical setup for FCS measurement. Fluorescence emitted from the perforated holes inside racetrack and waveguide.

4.4.2 Results and discussion

FCS is based on the autocorrelation function. The autocorrelation function for the function *F(t)* a certain time delay τ is given by the average value of the products

$$R(\tau) = \langle F(t)F(t+\tau)\rangle = \frac{1}{\tau}\int_0^T F(t)F(t+\tau)dt \qquad (4.2)$$

Since the only valuable contribution is given by the fluorescence intensity fluctuation $(t) = \langle F\rangle - F(t)$, it is possible to express the previous equation as

$$G'(\tau) = \frac{\langle F(t)F(t+\tau)\rangle}{\langle F\rangle\langle F\rangle} = 1 + \frac{\langle \delta F(0)\delta F(\tau)\rangle}{\langle F\rangle^2} \quad (4.3)$$

or as the autocorrelation function of fluorescence fluctuation:

$$G(\tau) = \frac{\langle \delta F(0)\delta F(\tau)\rangle}{\langle F\rangle^2} \quad (4.4)$$

The interpretation of the data is determined by the correct theoretical model for the description of the fluorescence and its fluctuation. Generally speaking, fluorescence can be described according to the excitation field and the optical properties of the fluorophore.

$$F(t) = B \int CEF(r)I(r)C(r,t)dV \quad (4.5)$$

Where $CEF(r)$ is a measure of the collection efficiency of the instrument, while $I(r)$ and $C(r,t)$ describe the excitation intensity and the fluorophores' distribution, respectively. Finally, B is the brightness and is a propriety of the fluorescent probe:

$$B = q\sigma Q \quad (4.6)$$

Where *q* indicates the quantum efficiency for detection of the emitted photons, σ is the absorption cross-section and Q is the quantum yield for emission of the fluorophore.

In standard FCS scheme [15] the excitation/detection volume are coincident and determined by laser (gaussian beam) focused with an objective. The brightness profile can be approximated as a three dimensional Gaussian and the detection profile of the instrument can be calculated considering CEF(r) and I(r) together. Briefly,the autocorrelation function for the intensity fluctuations can be written as

$$G(\tau) = \frac{B^2 \iint p(r)p(r')\langle \delta C(r,0)\delta C(r',\tau)\rangle dVdV'}{|BC \int p(r)dV|^2} \quad (4.7)$$

In the most easy and common application of the FCS techniques, one is interested in the analysis of translational diffusion, for which the autocorrelation function can be simplified as

$$G(\tau) = G(0)D(\tau) = G(0)\left(1 + \frac{\tau}{\tau_D}\right)^{-1}\left(1 + \left(\frac{s}{u}\right)^2 \frac{\tau}{\tau_D}\right)^{-1/2} \quad (4.8)$$

Where *s* and *u* are geometrical parameters of the observed volume, τ_D is the diffusion time, given by

$$\tau_D = s^2/4D \quad (4.9)$$

And G(0) indicate the intercept, and is related to the number of particles in the excitation volume and the detection profile γitself:

$$G(0) = \gamma/N \tag{4.10}$$

For a Gaussian volume, the detection profile is set as $= 0.35$, thus the intercept in condition of single particle in the volume is given for $G(0) = 0.35$.

In order to get confidence with the FCS technique, I decided to start with the most standard and clear configuration: the "classic confocal configuration", with excitation volume defined by focused laser by an objective and collected by the same objective. Under these conditions, the *100 pg/mL* concentration solution was evaluated as the optimal condition to obtain, on average, single particle in the detection volume (Figure 38.a).

The ring resonator platform was tested. FCS has been performed on holes of different size, exploring a wide range of concentrations. Switching to more confined volumes has two main consequences. First, in order to have a measurable quantity of molecules within the excitation volume, it is necessary to increase the total concentration of the solution under analysis. Second, the spatial confinement induces a variation in the diffusion motion of the molecules, increasing the decay time of the curve τ. Although the curves obtained have a not negligible noise, possibly due to the low fluorescence signal of the molecule inside the hole and fluorescence of the molecules in solution excited by the far field scattered from the hole, it is possible to find confirmation of the theorized reduction of the velocity of the molecule diffusion (potential trapping) inside the hole.

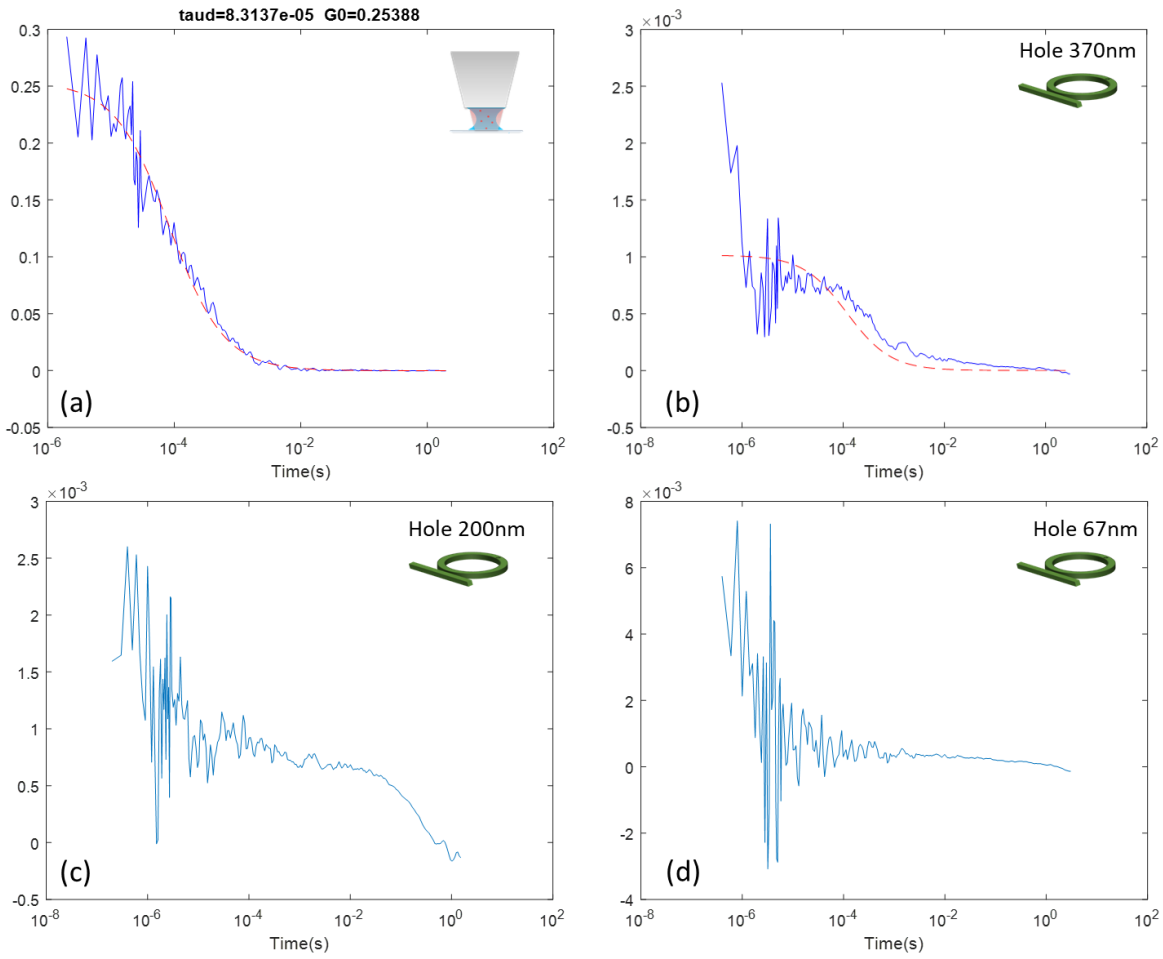

Figure 38 - FCS curves for ATTO633-NHS molecule in different conditions. (a) Free molecules in water solution. The parameters obtained from the fitted curve reveal a single molecule condition with concentration of 100 pg/mL. (b)-(d) FCS curves obtained from waveguides with holes of different diameter. Solution at 200ng/mL in (b) and 2 ug/mL in (c) and (d). Panel (b) reports the curve for the standard FCS curve with single exponential proving that the model does not fit the data.

It is important to highlight that the waveguide scheme differs significantly from the classical model for FCS. In standard FCS scheme [15] the excitation/detection volume are coincident and determined by laser (gaussian beam) focused with an objective. In order to better understand the FCS curves obtained, it is necessary to develop a theoretical model that describes the system under investigation. From the brief theoretical description of the FCS measurements proposed at the beginning of the paragraph, it is possible to identify the main parameters that play a fundamental role in the standard model and differ considerably in the structure under analysis.

In order to model the system in use, one has to correctly describe the intensity profile inside the sub-wavelength volume (distribution and near field), together with the fluorophores distribution

that will be sensitive to the restricted boundary conditions. Furthermore, as can be seen in eq. 4.5 that the collection efficiency of the system plays a fundamental role. In the configuration adopted during this measurements, the collection efficiency is limited also by geometrical factors. The near field excitation is much more efficient in exciting the molecules inside the hole, but on the other side also their emission is confined inside the hole. Thus the detection of the fluorescence in far field (as in our case) is limited by the size of the hole and the component near field/far field. In solution, the fluorophores are randomly oriented. In case of polarized excitation, only fluorophores whose absorption transition dipole is parallel to the excitation vector will be excited. Fluorescence emission occurs at times determined by the characteristic lifetime of each fluorophore, but typically about 1-10 ns. During this time, the rotational diffusion to which each fluorophore in solution is subjected causes the multiple rotation of each molecule, thus the orientation of the emission is randomized. The fluorescence is, in other words, almost isotropic and can occur in every direction. Considering the whole range of direction possible for the fluorescence emission, only a small portion will be contained in the solid angle defined by the hole's size and able to "escape" from the hole' confinement in order to be detected from the objective.

It is necessary to find the right balance between wettability of the system and dispersion of radiation from the hole as scattering. If on one side bigger hole allow better wettability and stronger optical signal, on the other side a big hole increases the far field excitation of molecules outside the hole. It is therefore necessary to reduce the losses so as to further minimize the noise caused by the fluorescence emitted by fluorophores outside the hole (scattering losses). However, it should be noted that in principle, it is possible to distinguish the two contributions (near field and far field) from the autocorrelation curve. In fact, these two phenomena can be attributed to molecules that diffuse in different volumes and times. In the autocorrelation curve we can expect to see a first decay at shorter times related to molecules excited in far field, which move by diffusive motion in unconfined volume. A second decay at longer times is instead ascribable to the molecules in the point-like source (hole), assuming that they are subject to deceleration or trapping forces and therefore remain longer in the excitation volume.

A possibility in order to avoid the contribution coming from the fluorophores excited in the far field could be that of move back to the vertical configuration (paragraph 4.2.1). Indeed, in this configuration we will detect only the signal coupled to the waveguide from the fluorophores confined inside the hole.

[1] F. Ma, Y. Li, B. Tang, and C. Y. Zhang, “Fluorescent Biosensors Based on Single-Molecule Counting,” *Acc. Chem. Res.*, vol. 49, no. 9, pp. 1722–1730, 2016.

[2] K. Hassler *et al.*, “Total internal reflection fluorescence correlation spectroscopy (TIR-FCS) with low background and high count-rate per molecule,” *Opt. Express*, vol. 13, no. 19, pp. 7415–7423, 2005.

[3] L. Lanzanò *et al.*, “Measurement of nanoscale three-dimensional diffusion in the interior of living cells by STED-FCS,” *Nat. Commun.*, vol. 8, no. 1, pp. 1–9, 2017.

[4] M. Foquet, J. Korlach, W. R. Zipfel, W. W. Webb, and H. G. Craighead, “Focal Volume Confinement by Submicrometer-Sized Fluidic Channels than 1 μ m were fabricated in fused silica for high-,” *Anal. Chem.*, vol. 76, no. 6, pp. 1618–1626, 2004.

[5] A. Lewis *et al.*, “Near-field optics: From subwavelength illumination to nanometric shadowing,” *Nat. Biotechnol.*, vol. 21, no. 11, pp. 1378–1386, 2003.

[6] J. Chen *et al.*, “High-throughput platform for real-time monitoring of biological processes by multicolor single-molecule fluorescence,” *Proc. Natl. Acad. Sci.*, vol. 111, no. 2, pp. 664–669, 2014.

[7] J. Sobek *et al.*, “Single-molecule DNA hybridisation studied by using a modified DNA sequencer: A comparison with surface plasmon resonance data,” *Methods Appl. Fluoresc.*, vol. 4, no. 1, p. 15002, 2016.

[8] M. J. Levene, “Zero-Mode Waveguides for Single-Molecule Analysis at High Concentration,” vol. 299, no. 5607, pp. 682–687, 2003.

[9] K. T. Samiee, J. M. Moran-Mirabal, Y. K. Cheung, and H. G. Craighead, “Zero mode waveguides for single-molecule spectroscopy on lipid membranes,” *Biophys. J.*, vol. 90, no. 9, pp. 3288–3299, 2006.

[10] J. Eid *et al.*, “Single Polymerase Molecules,” *Science*, vol. 323, no. January, pp. 133–138, 2009.

[11] S. M. Christensen *et al.*, “Monitoring the Waiting Time Sequence of Single Ras GTPase Activation Events Using Liposome Functionalized Zero-Mode Waveguides,” *Nano Lett.*,

vol. 16, no. 4, pp. 2890–2895, 2016.

[12] C. Zhao, Y. Liu, J. Yang, and J. Zhang, “Single-molecule detection and radiation control in solutions at high concentrations via a heterogeneous optical slot antenna,” *Nanoscale*, vol. 6, no. 15, pp. 9103–9109, 2014.

[13] P. Ponzellini, X. Zambrana-Puyalto, N. Maccaferri, L. Lanzanò, F. De Angelis, and D. Garoli, “Plasmonic zero mode waveguide for highly confined and enhanced fluorescence emission,” *Nanoscale*, pp. 17362–17369, 2018.

[14] S. R. Aragón and R. Pecora, “Fluorescence correlation spectroscopy as a probe of molecular dynamics,” *J. Chem. Phys.*, vol. 64, no. 4, pp. 1791–1803, 1976.

[15] J. R. Lakowicz, *Principles of Fluorescence Spectroscopy*. 2006.

[16] G. Krichevsky, Oleg and Bonnet, “Fluorescence correlation spectroscopy : the technique,” *Reports Prog. Phys.*, vol. 65, pp. 251–297, 2002.

[17] H. A. Bethe, "Theoryof Diffraction by Small Holes," *Phys. Rev.*, vol. 66, no. 7-8, pp.163-182, 1944.

[18] C. J. Bowkamp, "On Bethe's theory of diffraction by small holes," *Philips Res. Rep.*, vol. 5, no. 3, pp. 321-332, 1950.

[19] C. Genet and T. W. Ebbesen, "Light in tiny holes," *Nature*, vol. 445, pp. 39-46, 2007.

Conclusion & Future Perspective

In conclusion, an innovative design was presented for a biosensor capable of detecting single particle on chip. The biosensor was designed to combine integrated optics with the most widely used assay technology, fluorescence-based assays. The structure consists of a ring resonator of dielectric material excited by a bus waveguide on chip, the novelty element consists of a through hole that crosses the resonant structure throughout its thickness. This, of remarkably sub-wavelength size, acts as an on-chip point-like source. Therein, the field is extremely confined and uniform compared to other nanostructured structures proposed in literature (for example not perforated whispering gallery mode resonators and photonic crystal cavities). In order to obtain a hole of nanometric size with extreme precision and without damaging the photonic structure, advanced nanofabrication techniques available in the cleanroom facility of the IIT have been exploited.

A full 3D finite element method simulation of the optical properties of the structure has been proposed and the performances in terms of sensitivity and detection limit of the new perforated structure with respect to the standard model have been theoretically compared.

The optical characterization of the sub-wavelength source created in the resonant structure has been carried out. By excitation with a supercontinuum laser source, the possibility of spectrally resolve the splitting induced by the defect inserted in the resonant structure (the hole) has been verified, even if within certain instrumental limits.

A configuration has been proposed also to perform measurements of a single particle in solution by monitoring the shift of the active resonant mode. This technique would allow single particle measurements to be made in a label-free configuration. Moreover, using the inactive resonant mode as a reference, a self-referenced measurement method and further reduction of the noise are obtained.

The point-like source was characterized in terms of optical confinement, evaluating the signal-to-noise ratio with respect to the background, and discussing the advantages of using a resonant structure as opposed to a linear guide.

The use of the structure in conjunction with the fluorescence assays was then addressed. The functionality of the system as a tool for detecting single particle on chip in dense media, based on the model of nano-apertures and in accordance with experimental conditions closer to biological ones, was then verified.

Single particle measurement has been verified for both: resonant structure and straight waveguide. Again, a comparison of the two solutions was made.

In order to further characterize the on-chip point-like source, preliminary fluorescence correlation spectroscopy measurements were carried out. The application of the technique is however limited by certain parameters. Indeed although the near field excitation allows to efficiently excite the particles in a confined volume, also the emission of these particles will remain confined inside the hole and within the configuration adopted (detection in far field by a water immersion objective at high numerical aperture) the efficiency of the detection system is limited by the size of the source itself. It is also highlighted the need for an accurate model that describes the system to interpret correctly the FCS curves obtained and verify eventual trapping or deceleration of the particle within the volume. The model should for example take into account the nature of the excitation field (near field in sub-wavelength volume) and the forces acting on the particles/molecules at the nanoscale.

The presented system falls within a hot topic in terms of both fundamental and industrial research. Within the vast field of biosensors, a very interesting area is the detection of single particles in complex media, i.e. liquid biopsy. The reported results demonstrate the potential of the modeled structure as an emerging technology in this sector, thus we can identify promising commercial perspectives of the proposed system. Liquid biopsy indicates the ability to perform analyses to detect diseases (from infections to cancer) from a sample of biological fluid. It is still an open issue, characterized from a huge interest in fundamental and industrial research for its market and social repercussions. For example, liquid biopsy is emerging as a valid alternative to tumor tissue biopsies for cancer diagnosis, finding application in routine monitoring and prognostication of circulating tumor biomarkers. Points of strength of these biosensors are their low costs, high sensitivity and able to perform multiplexing analysis. Leveraging on the well-developed silicon photonics technology and through the use of fluorescence tests together with the novelty point introduced in the resonating structure, our device promises to meet the above requirements. Further

perspectives for this project is to investigate its potentialities from a commercial point of view, going for a complete characterization of the system and its validation as bioassay.